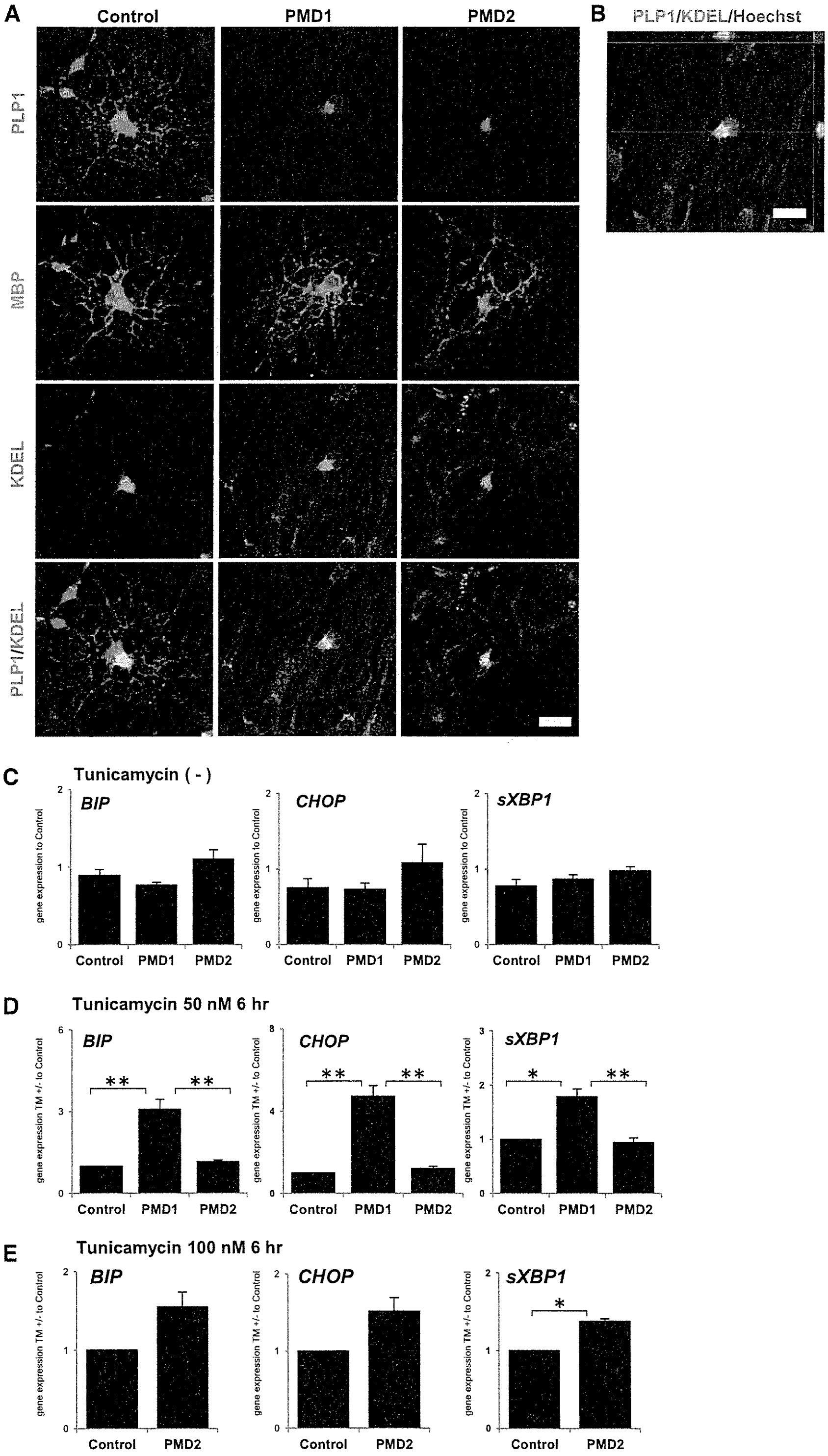

Figure 4. Involvement of ER Stress in PMD-Derived Oligodendrocytes

(A) Representative immunocytochemistry image for PLP1, the OL marker MBP, and the ER marker KDEL. In the control iPSC-derived mature OLs, the PLP1 protein localized to both the ER (KDEL) and membrane, whereas in the PMD iPSC-derived OLs, the mutant PLP1 protein only localized to the ER. The scale bar represents 20 μm.

(B) Three-dimensional image of mature OLs derived from PMD1 iPSCs showing colocalization of the mutant PLP1 protein and KDEL via confocal laser scanning microscopy. The scale bars represent 20 μm.

(C) Quantitative RT-PCR analyses of the expression of ER stress markers in O4$^+$ cells. The data are presented as the expression relative to that in iPSCs. No significant differences were observed between the control iPSC (201B7, WD39, and TIG121) and PMD iPSC (PMD1-7, PMD1-15, and PMD1-27 and PMD2-6, PMD2-10, and PMD2-22)-derived cells (n = 5; mean ± SEM; independent experiments; t test).

(D) Quantitative RT-PCR analyses of the expression of ER stress markers in tunicamycin-treated (50 nM; 6 hr) O4$^+$ cells relative to untreated O4$^+$ cells. A higher level of stress susceptibility was detected in PMD1 (PMD1-7, PMD1-15, and PMD1-27) than in control (201B7, WD39, and TIG121) and PMD2 (PMD2-6, PMD2-10, and PMD2-22; n = 5; mean ± SEM; independent experiments; $^*p < 0.05$; $^{**}p < 0.01$; Mann-Whitney's U test).

(E) Quantitative RT-PCR analyses of the expression of ER stress markers in tunicamycin-treated (100 nM; 6 hr) O4$^+$ cells relative to untreated O4$^+$ cells. PMD2 iPSC (PMD2-6, PMD2-10, and PMD2-22)-derived OLs showed significantly higher expression levels of spliced *XBP1* than control iPSC (201B7, WD39, and TIG121)-derived OLs (n = 3; mean ± SEM; independent experiments; $^*p < 0.05$; t test).

the differentiation efficiency into oligodendrocyte lineage cells was unchanged between PMD and control (Figure 3C), considering that anti-O4 and anti-MBP antibodies stain both apoptotic and live OLs (Figures 5A and 5C), the increased levels of apoptosis resulted in decreased numbers of live OLs in PMD iPSC-derived cultures.

Because previous reports have indicated the neurotrophic actions of PLP1 (Griffiths et al., 1998; Yin et al.,

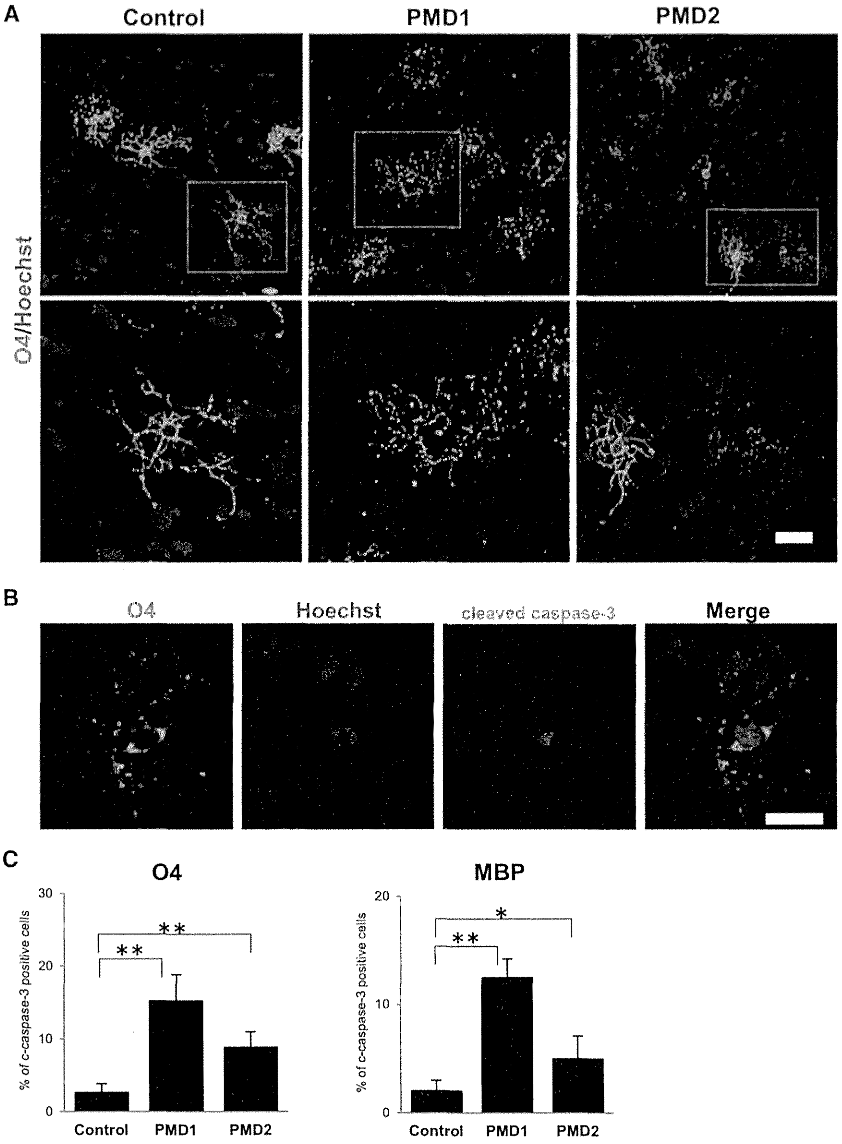

Figure 5. Enhanced Apoptosis in PMD iPSC-Derived Oligodendrocytes

(A) Morphological differences in OLs. Immunocytochemical analysis of iPSC-derived OLs for OLs marker (O4) and nuclei (Hoechst). The OLs showed a uniform appearance in the control iPSC-derived cells but showed scattered morphologies in the PMD iPSC-derived cells. The scale bar represents 40 μm.

(B) Representative immunocytochemical images of apoptotic OLs using markers for apoptosis (cleaved caspase-3) and OLs (O4). OLs ($O4^+$ or MBP^+) that were both positive for cleaved caspase-3 and showed nuclear condensation or fragmentation were considered apoptotic OLs. The scale bar represents 40 μm. c-caspase-3, cleaved caspase-3.

(C) Quantitative analysis of the number of apoptotic OLs. The number of apoptotic cells was higher in the PMD1 (PMD1-7, PMD1-15, and PMD1-27) and PMD2 iPSC (PMD2-6, PMD2-10, and PMD2-22)-derived OLs than control iPSC (201B7, WD39, and TIG121)-derived OLs ($n = 9$; mean ± SEM; independent experiments; $^*p < 0.05$; $^{**}p < 0.01$; Mann-Whitney's U test).

2006), we next investigated whether apoptosis was induced in PMD patient-derived neurons. However, no cleaved caspase-3^+ neurons derived from either control or PMD iPSCs were observed (Figure S2C), suggesting that this increased apoptosis was specific to oligodendrocyte lineage cells in PMD in our iPSC-derived cultures.

Abnormal Myelin Structures and ER Morphologies Were Detected by Electron Microscopic Analysis

Finally, we focused on the myelinating properties of PMD iPSC-derived OLs, which represent the most characteristic pathogenic feature of PMD. Because different types of neural cells, including neurons and astrocytes, in addition to OLs, were derived in our cultures, neuron-glial interactions could be observed and neuron myelination by the iPSC-derived OLs could be analyzed in situ. In immunocytochemical analysis of MBP and NF200 (neurofilament marker), parts of the neurofilament$^+$ neurites were wrapped by the MBP^+ process of iPSC-derived oligodendrocytes (Figure S3A). Thus, to evaluate the histological abnormality of the myelin structures in vitro, we performed transmission electron microscopy (TEM) analysis of ultrathin sections of the differentiated cells. The results showed that myelin structures with or without axons could be observed via TEM. Considering the neuronal processes wrapped by the MBP^+ process of iPSC-derived OLs observed through immunocytochemistry, some of the axonal structures could have been lost during the fixation process for TEM.

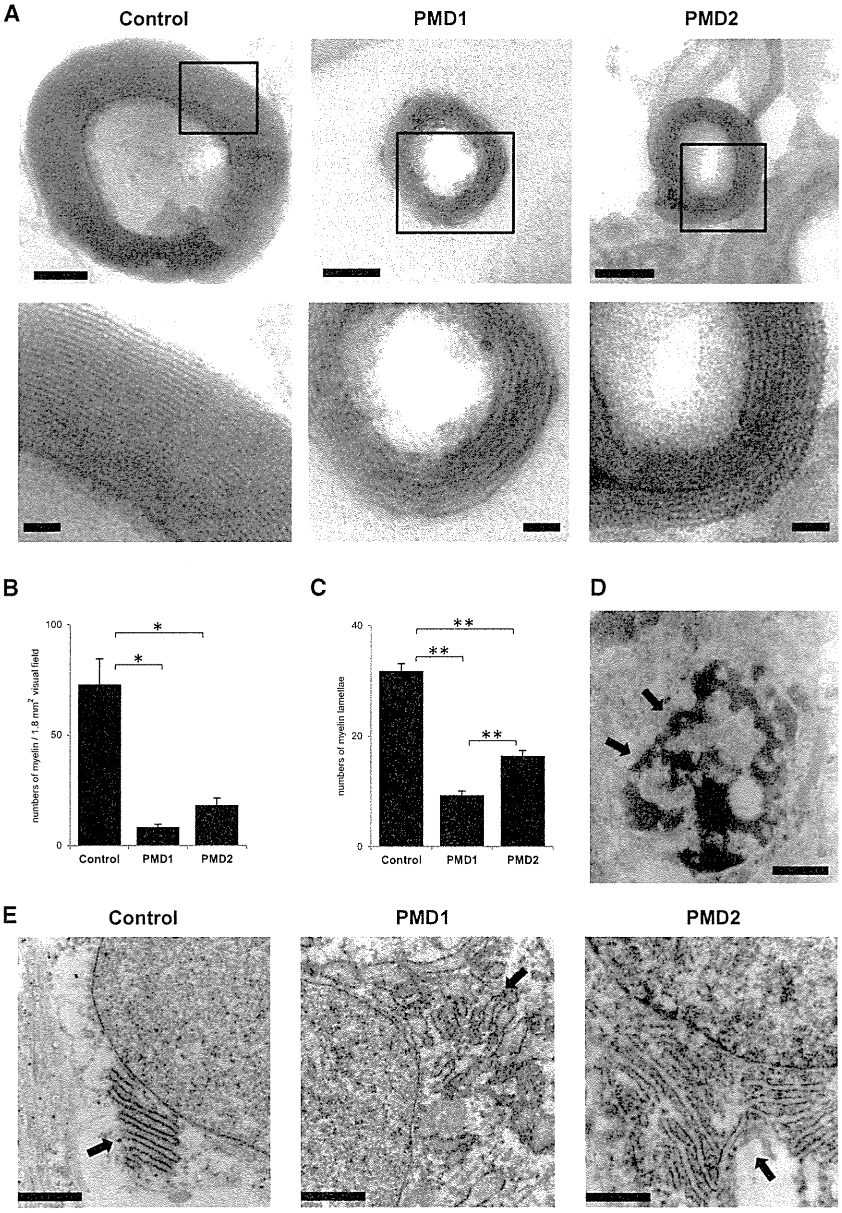

Figure 6. Electron Microscopic Analysis of PMD iPSC-Derived Cells

(A) TEM of iPSC-derived cells. The maximum number of normal myelin lamella was greater than 30 in the control iPSC-derived myelin sheaths. In contrast, a limited number of myelin lamella was observed in the PMD iPSC-derived myelin sheaths. High-magnification images are also shown in the lower panel. The scale bars represent 100 nm (upper panels) and 20 nm (lower panels).

(B) Quantitative analysis of the numbers of myelin structures. We counted the numbers of myelin structures per visual field of EM images (approximately 1.8 mm^2) for the myelination frequency. The frequency of myelin formation was significantly decreased in both PMD1 (PMD1-7, PMD1-15, and PMD1-27) and PMD2 (PMD2-6, PMD2-10, and PMD2-22) iPSC-derived OLs (n = 3; mean ± SEM; independent experiments; $^*p < 0.05$; t test).

(C) Quantitative analysis of the numbers of myelin lamellae. We counted the numbers of major dense lines per myelinated fiber for the thickness of myelin, and the average of the numbers of myelin lamellae in the top ten myelin sheaths are presented. The thickness of the myelin sheath was greatly reduced in both PMD1 (PMD1-7, PMD1-15, and PMD1-27) and PMD2 (PMD2-6, PMD2-10, and PMD2-22) iPSC-derived OLs (n = 3; mean ± SEM; independent experiments; $^{**}p < 0.01$; t test).

(D and E) Histological abnormalities detected in PMD iPSC-derived cells via TEM. Apoptotic cells with fragmented nuclei (arrow in D) were frequently detected among the PMD-iPSC-derived cells (D). The scale bar represents 1 μm. Dilations of ER intermembrane spaces were also observed (E). The scale bars represent 0.5 μm.

Although we stained with antibodies against NAV1.6 (nodes) and CASPER (paranodes), we could not detect any significant staining in our cultures. This may suggest immature myelination in the present culture conditions.

Notably, mature myelin structures with thick myelin lamella ~30 layers were observed in the control cultures. In contrast, in the PMD iPSC-derived cultures, a limited number of myelin structures with thin myelin lamella ~15 layers were observed (Figure 6A). The frequency of myelin formation and thickness of the myelin sheath were significantly decreased in both PMD1 and PMD2 iPSC-derived OLs (Figures 6B and 6C).

In addition, several types of histological abnormalities were detected in the PMD cells. Apoptotic cells exhibiting nuclear condensation were frequently observed among the PMD iPSC-derived cells, in contrast to that observed in those derived from control iPSCs (Figure 6D). Moreover, aberrant ER morphologies, such as dilation of the ER intermembrane space (Fan et al., 2013; Lim et al., 2011), were found in the PMD iPSC-derived cells (Figure 6E). These results indicate that PMD iPSC-derived OLs develop a poor myelin structure and subsequently die, supporting the involvement of ER stress in the pathogenesis of PMD.

DISCUSSION

In this study, we established PMD-specific human iPSCs from two patients with different clinical severity and different missense mutations of *PLP1*. One mutation is in the transmembrane domain (PMD1) and the other is in the extracellular domain (PMD2), both of which differ from those in the previously reported PMD animal models. And we generated patient-specific OLs. This model enables an investigation of the correlations between the molecular pathophysiology of PMD and various cell biological phenomena, including OL differentiation, myelination, and apoptosis in patient-derived live OLs through morphological, biochemical, and molecular biological methods. These analyses could not be achieved using conventional disease models.

Although there are several reported methods for inducing OPCs from human ESCs (Hu et al., 2009; Izrael et al., 2007; Kang et al., 2007), these methods have difficulties in reproducibility, making it difficult to obtain sufficient amounts of mature OLs for analysis. In the present study, we developed an improved neural differentiation protocol for human pluripotent stem cells by utilizing an EB-neurosphere method involving dual Smad inhibition in combination with a GSK3 inhibitor to facilitate differentiation into NS/PCs more efficiently and reproducibly. In addition, the use of T3, ciliary neurotrophic factor (CNTF), and leukemia inhibitory factor (LIF) was beneficial for differentiation into OLs. Using this method, we achieved stable differentiation of several human iPSC clones into OLs in a similar manner to that reported in a recent study (Wang et al., 2013). Remarkably, our culture procedure enabled recapitulation of myelin formation in human iPSC (hiPSC)-derived neurites and OLs in vitro in a single-culture system without coculturing with other cells, such as rodent hippocampal neurons, as previously reported (Kang et al., 2007). Thus, this study reports a successful in vitro myelination assay using human iPSC-derived neurons and OLs.

Another important finding of this study was that the differentiation of PMD iPSCs into OLs well-recapitulated the progression of PMD pathogenesis in vitro. Although the PMD-specific iPSCs induced abundant MBP^+ mature OLs, myelination was substantially less frequent and limited lamella formation was observed. These results suggest that incomplete maturation and limited survival of OLs rather than a failure to differentiate into OLs is responsible for PMD pathogenesis. However, the cause of OL degeneration and dysmyelination observed in PMD is unclear. Some previous reports have demonstrated the involvement of ER stress in the pathogenesis of PMD associated with missense mutations in the *PLP1* gene. Analyses using cell lines, such as cos7 cells transfected with wild-type or mutant *PLP1* genes, have shown that wild-type PLP1 protein is synthesized in the ER and transported to the cell surface, whereas mutant PLP1 proteins are arrested in the secretory pathway at an early stage and accumulate in the ER (Gow et al., 1994). In the CNS of PMD model mice, such as msd and rsh mice, mutant PLP1 proteins are largely confined to the perinuclear region of OLs and involved in the UPR (Gow et al., 1998). These reports suggest the involvement of ER stress in PMD pathogenesis. In the present study, accumulation of misfolded mutant PLP1 proteins in the ER and high susceptibility to ER stresses in the PMD1 and PMD2 cells were observed. This increased susceptibility to ER stresses or other cellular response could have resulted in the apoptosis of PMD iPSC-derived OLs and immature/incomplete myelination.

In addition, we detected differences between PMD1 and PMD2 cells. The differences of susceptibility to ER stresses and the thickness of the myelin sheath were consistent with the different levels of clinical severity of the two patients. The correlations between different clinical severity, different missense mutations, and different pathogenic changes have not previously been reported by conventional disease models. These results suggest that this PMD model accurately recapitulates disease pathophysiology not only qualitatively but also in terms of the degree of disease progression, although how the different point mutations affect the degree of the observed phenotype must be clarified. Accordingly, we propose models for a "proof-of-concept" of PMD pathogenesis based on the endogenous mutations found in PMD iPSC-derived OLs. The present findings cannot be generalized to PMD as a whole because the more common *PLP1* duplication was not included; therefore, we will investigate the pathogenesis of PMD with *PLP1* duplications in the future.

The current study represents the a demonstration of pathogenic changes in PMD patients with *PLP1* missense mutations using disease-specific, human iPSC-derived OLs. This model faithfully reproduces the pathophysiology observed in the CNS of PMD patients, which is difficult to identify through conventional experiments. Moreover, our results demonstrate the usefulness of iPSC-derived OLs for the analysis of the pathogenic processes of dysmyelinating human neurological disorders and the development of novel therapeutic agents for their treatment.

EXPERIMENTAL PROCEDURES

Isolation of Human Skin Fibroblasts and Generation of iPSCs

HDFs from the dermis of a 1-year-old Japanese male patient and HDFs from the dermis of a 20-year-old Caucasian male patient (Coriell Institute: GM09546) were used to establish PMD1-iPSCs (PMD1-7, 1-15, and 1-27) and PMD2-iPSCs (PMD2-6, 2-10, and

2-22), respectively. Additional control cell lines used in this study included 201B7 (control A, established from HDFs [Cell Applications] from the dermis of a 36-year-old Caucasian female; Takahashi et al., 2007), WD39 (control B, established from HDFs from the dermis of a 16-year-old Japanese female; Imaizumi et al., 2012), and TIG121 (control C, established from HDFs from the dermis of an 8-month-old Japanese male [Japan Health Sciences Foundation]). All of the human iPSC clones were established through the retroviral transduction of four transcription factors (*SOX2*, *OCT4*, *KLF4*, and *c-MYC*) into HDFs as described previously (Takahashi et al., 2007) and evaluated based on the expression of pluripotent markers, the silencing of retroviral transgenes, and teratoma formation assays as described previously (Ohta et al., 2011). We used three clones for each group for further analysis: control (201B7, WD39, and TIG121), PMD1 (1-7, 1-15, and 1-27), and PMD2 (2-6, 2-10, and 2-22). The data from the three clones were combined in each figure, and the data are shown as the average of the three clones. All of the experimental procedures for iPSC production were approved by the ethics committee of the Keio University School of Medicine (approval number: 20-16-18).

Culture and In Vitro Differentiation of Human iPSCs

hiPSCs were grown on mitomycin-C-treated SNL murine fibroblast feeder cells in gelatin-coated (0.1%) tissue culture dishes. The hiPSCs were maintained in standard hESC medium (Dulbecco's modified Eagle's medium [DMEM]/F12 [Sigma] containing 20% KnockOut serum replacement [KSR; Life Technologies], nonessential amino acids [NEAA], 0.1 mM 2-mercaptoethanol [Sigma], and 4 ng/ml fibroblast growth factor 2 [FGF-2] [PeproTech]) at 37°C in a humidified atmosphere of 3% CO_2.

For in vitro differentiation, iPSC colonies were detached from the feeder layers en bloc using a dissociation solution (0.25% trypsin, 100 μg/ml collagenase IV [Invitrogen], 1 mM $CaCl_2$, and 20% KSR; day 0) and cultured in suspension in bacteriological dishes to form EBs in a humidified atmosphere of 3% CO_2. From day 1 to 4 of EB formation, 3 μM dorsomorphin (Sigma), 3 μM SB431542 (Tocris Bioscience), and 3 μM BIO ((2′Z, 3′E)-6-bromoindirubin-3′-oxime; Sigma) were added. In addition, 1 μM retinoic acid (Sigma) and 1 μM purmorphamine (Calbiochem) were added on days 4 and 7, respectively, and maintained thereafter until day 16 (EB dissociation). The medium was changed every 2 days. On day 16, the EBs were enzymatically dissociated into single cells using TrypLE Select (Life Technologies), and the dissociated cells were cultured in suspension at a density of 1×10^5 cells/ml in proliferation medium consisting of serum-free medium (media hormone mix [MHM]; Okada et al., 2008) supplemented with 2% B27 supplement (Invitrogen), NEAA, 1 μM purmorphamine, 60 ng/ml T3 (Sigma), 10 ng/ml PDGF-AA (PeproTech), 20 ng/ml FGF, 10 ng/ml epidermal growth factor (PeproTech), 10 ng/ml insulin growth factor 1, and 10 ng/ml neurotrophin-3 (R&D Systems) in a humidified atmosphere of 5% CO_2. The medium was changed every 4~6 days for approximately 15~20 days to form the first neurospheres. To passage neurospheres, the first neurospheres were dissociated in the same manner as described above and cultured at a density of 1×10^5 cells/ml in proliferation medium without purmorphamine for approximately 15~20 days. To assay neurosphere differentiation, undissociated 5–7 neurospheres were plated onto coverslips 10 mm in diameter coated with poly-L-ornithine (Sigma) and growth-factor-reduced Matrigel (50× dilution, thin coated; Invitrogen), and cultured in differentiation medium that consisted of MHM supplemented with 2% B27 supplement, NEAA, 60 ng/ml T3, 10 ng/ml hLIF (Millipore), and 25 ng/ml CNTF (R&D Systems) for 2–6 weeks in a humidified atmosphere of 5% CO_2. Half of the medium was changed every 2 or 3 days. For the quantitative analysis of the differentiation efficiency into OL lineage cells, the numbers of neurosphere colonies containing more than 40 marker-positive cells (≥40 cells, oligodendrocyte [++]), those containing less than 40 marker-positive cells (1–39 cells, oligodendrocyte [+]), and those without marker-positive cells (oligodendrocyte [−]) were counted and are presented as the percentage of total neurosphere colonies. To examine the expression of ER-stress markers, $O4^+$ differentiated cells were purified 4 weeks after the attachment of the neurospheres using MACS technology with an anti-O4 antibody.

Direct Sequencing and Pyrosequencing Analysis of the *PLP1* Gene

Genomic DNA was extracted from peripheral blood samples (leukocytes) from PMD1 and from HDFs and iPSCs from both PMD1 and PMD2. For direct sequencing of the mutations in the *PLP1* gene in PMD1, fragments of the promoter regions (5′ UTR) and all seven exons of the *PLP1* gene were amplified via PCR. The PCR primers and cycling conditions employed for direct sequencing are listed in Table S1. For pyrosequencing analysis of the mutations in the *PLP1* gene in HDFs and iPSCs, fragments containing the PMD1 mutation (c.757 T > A in exon 6) and PMD2 mutation (c.643 C > T in exon 5) were amplified via PCR using forward primers and biotinylated reverse primers. Pyrosequencing analyses were performed following the manufacturer's instructions (Pyromark Q24; QIAGEN). The PCR primers and cycling conditions applied for pyrosequencing analysis are listed in Table S2.

RNA Isolation and RT-PCR

RNA isolation and real-time quantitative RT-PCR were performed as previously described using SYBR Premix ExTaq II and the MX3000P Real-Time PCR system (Stratagene; Okada et al., 2004, 2008). The amount of cDNA was normalized to that of human-specific *β-ACTIN* mRNA.

For the analysis of the expression of retroviral transgene in iPSCs, HDFs 7 days after the retroviral introduction (day 11 of the protocol) of four genes (*SOX2*, *OCT4*, *KLF4*, and *c-MYC*) were used as the positive control (*SOX2* tg, *OCT4* tg, *KLF4* tg, and *c-MYC* tg). The data are presented as the copy numbers of mRNA for each transgene. As for the analyses of *NANOG*, *SOX1*, *BRACHYURY*, *SOX17*, *βIII tubulin*, *GFAP*, *CNP*, and ER stress marker (*BIP*, *CHOP*, and *spliced XBP1)*, data are presented as the relative expression to that in control. The applied primer sequences and PCR cycling conditions are listed in Table S3.

Immunocytochemical Analysis

For immunocytochemical analysis, cells were fixed with 4% paraformaldehyde for 30 min at room temperature. After blocking in blocking buffer (PBS containing 10% normal goat or donkey serum and 0.3% Triton X-100) for 1 hr at room temperature, the cells were incubated with primary antibodies at 4°C overnight. For O4 staining, we used blocking buffer without Triton X-100. After three washes with PBS, the cells were incubated with Alexa 488-, Alexa 555-, or Alexa 647-conjugated secondary antibodies (Life Technologies) for 1 hr at RT. Nuclei were stained with 10 μg/ml Hoechst 33258 (Sigma). After washing with PBS, the cells were mounted on slides and examined with a universal fluorescence microscope (Axiophoto; Carl Zeiss) or confocal laser scanning microscope (LSM700; Carl Zeiss). The primary antibodies used in these analyses were as follows: NANOG (1:100; ReproCELL), OCT4 (1:500; Santa Cruz Biotechnology), OLIG2 (1:1,000; R&D Systems), PDGFRα (1:2,000; Santa Cruz Biotechnology), NG2 (1:2,000; Millipore), O4 (1:5,000; Millipore), MBP (1:1,000; Serotec), β-III-tubulin (1:1,000; Sigma), NF200 (1:1,000, Millipore), GFAP (1:4,000, Dako), KDEL (Abcam), PLP1 (1:30,000; gifted from Masayuki Itoh [National Center of Neurology and Psychiatry] recognizes PLP1, but not DM20), KI67 (1:10,000, Abcam), and cleaved caspase 3 (1:1,000, Cell Signaling Technology).

Teratoma Assay

Undifferentiated iPSCs (5×10^5 cells) were injected into the testes of 8-week-old male nonobese diabetic (NOD)/severe combined immunodeficiency (SCID) mice (Charles River Laboratories) as described previously (Ohta et al., 2011). Eight weeks after injection, the resultant tumors were dissected and fixed with 4% paraformaldehyde. Paraffin-embedded tissue sections were produced, and hematoxylin and eosin (H&E) staining was performed. Images were obtained using a BZ-9000 microscope (Keyence).

Transmission Electron Microscopy

For TEM analysis, neurospheres and cells in dishes were fixed with 2.5% glutaraldehyde in 50 mM phosphate buffer (PB) overnight at 4°C. After washing twice in 0.1 M PB, these samples fixed with 1% osmium tetroxide for 90 min, dehydrated through ethanol, and embedded in Epon. The neurospheres were dissected and fixed on the stage, followed by the preparation of ultrathin sections with a thickness of 70 nm using an ultramicrotome (Leica Microsystems). The sections were subsequently stained with uranyl acetate and lead citrate for 10 and 12 min, respectively. Finally, the sections were observed under a transmission electron microscope (JEOL model 1230), and images were captured with Digital Micrograph 3.3 (Gatan). For the quantitative analysis of myelination, the number of myelin lamellae, which is the number of major dense lines per myelinated fibers, was counted to assess myelin thickness and the number of myelinated fibers per visual field of electron microscopy (EM) images (approximately 1.8 mm^2) was counted to assess myelination frequency.

SUPPLEMENTAL INFORMATION

Supplemental Information includes three figures and three tables and can be found with this article online at http://dx.doi.org/10.1016/j.stemcr.2014.03.007.

ACKNOWLEDGMENTS

We are grateful to Prof. F. Urano (Washington University School of Medicine) for valuable comments and analysis of ER stress, Prof. M. Amagai (Keio University) for skin biopsies, I. Kuki (Osaka City General Hospital) for providing patient medical information, M. Itoh (National Center of Neurology and Psychiatry) for providing PLP1 antibody, T. Nagai (Keio University) for assistance with the TEM analyses, N. Kuzumaki (Keio University) for technical assistance, and all of the members of H.O.'s laboratory for their encouragement and support. This work was supported by funding from the Project for the Realization of Regenerative Medicine and Support for Core Institutes for iPS Cell Research from the Ministry of Education, Culture; Support for the Core Institutes for iPS Cell Research from the Ministry of Education, Culture, Sports, Science and Technology of Japan (MEXT; to H.O.); and a Grant-in-Aid for the Global COE Program from MEXT to Keio University. This work was also supported by a Grant-in-Aid for Young Scientists (B) from MEXT, a Keio University Grant-in-Aid for the Encouragement of Young Medical Scientists to Y.K.-N. from the Kanrinmaru-Project at Keio University, a Grant-in-Aid for Young Scientists (A) and a Grant-in-Aid for Scientific Research on Innovative Areas (Foundation of Synapse Neurocircuit Pathology) from MEXT, and JST-CIRM Collaborative Research Program funding awarded to Y.O. H.O. is a scientific consultant for SanBio, Inc., Eisai, Co., Ltd., and Daiichi Sankyo, Co., Ltd. M.S. and A.N. are employed by Takeda Pharmaceutical Company Limited. S.Y. is a member without salary of the scientific advisory boards of iPierian, iPS Academia Japan, Megakaryon Corporation, and HEALIOS K. K. Japan.

Received: October 8, 2013
Revised: March 20, 2014
Accepted: March 20, 2014
Published: April 24, 2014

REFERENCES

Fan, J., Long, H., Li, Y., Liu, Y., Zhou, W., Li, Q., Yin, G., Zhang, N., and Cai, W. (2013). Edaravone protects against glutamate-induced PERK/EIF2α/ATF4 integrated stress response and activation of caspase-12. Brain Res. *1519*, 1–8.

Gencic, S., Abuelo, D., Ambler, M., and Hudson, L.D. (1989). Pelizaeus-Merzbacher disease: an X-linked neurologic disorder of myelin metabolism with a novel mutation in the gene encoding proteolipid protein. Am. J. Hum. Genet. *45*, 435–442.

Gow, A., and Lazzarini, R.A. (1996). A cellular mechanism governing the severity of Pelizaeus-Merzbacher disease. Nat. Genet. *13*, 422–428.

Gow, A., Friedrich, V.L., Jr., and Lazzarini, R.A. (1994). Many naturally occurring mutations of myelin proteolipid protein impair its intracellular transport. J. Neurosci. Res. *37*, 574–583.

Gow, A., Gragerov, A., Gard, A., Colman, D.R., and Lazzarini, R.A. (1997). Conservation of topology, but not conformation, of the proteolipid proteins of the myelin sheath. J. Neurosci. *17*, 181–189.

Gow, A., Southwood, C.M., and Lazzarini, R.A. (1998). Disrupted proteolipid protein trafficking results in oligodendrocyte apoptosis in an animal model of Pelizaeus-Merzbacher disease. J. Cell Biol. *140*, 925–934.

Griffiths, I., Klugmann, M., Anderson, T., Yool, D., Thomson, C., Schwab, M.H., Schneider, A., Zimmermann, F., McCulloch, M., Nadon, N., and Nave, K.A. (1998). Axonal swellings and degeneration in mice lacking the major proteolipid of myelin. Science *280*, 1610–1613.

Hodes, M.E., Aydanian, A., Dlouhy, S.R., Whelan, D.T., Heshka, T., and Ronen, G. (1998). A de novo mutation (C755T; Ser252Phe) in exon 6 of the proteolipid protein gene responsible for Pelizaeus-Merzbacher disease. Clin. Genet. *54*, 248–249.

Hu, B.Y., Du, Z.W., and Zhang, S.C. (2009). Differentiation of human oligodendrocytes from pluripotent stem cells. Nat. Protoc. *4*, 1614–1622.

Imaizumi, Y., Okada, Y., Akamatsu, W., Koike, M., Kuzumaki, N., Hayakawa, H., Nihira, T., Kobayashi, T., Ohyama, M., Sato, S., et al. (2012). Mitochondrial dysfunction associated with increased oxidative stress and α-synuclein accumulation in PARK2 iPSC-derived neurons and postmortem brain tissue. Mol. Brain *5*, 35.

Izrael, M., Zhang, P., Kaufman, R., Shinder, V., Ella, R., Amit, M., Itskovitz-Eldor, J., Chebath, J., and Revel, M. (2007). Human oligodendrocytes derived from embryonic stem cells: Effect of noggin on phenotypic differentiation in vitro and on myelination in vivo. Mol. Cell. Neurosci. *34*, 310–323.

Kang, S.M., Cho, M.S., Seo, H., Yoon, C.J., Oh, S.K., Choi, Y.M., and Kim, D.W. (2007). Efficient induction of oligodendrocytes from human embryonic stem cells. Stem Cells *25*, 419–424.

Lim, M.P., Devi, L.A., and Rozenfeld, R. (2011). Cannabidiol causes activated hepatic stellate cell death through a mechanism of endoplasmic reticulum stress-induced apoptosis. Cell Death Dis. *2*, e170.

Mikoshiba, K., Okano, H., Tamura, T., and Ikenaka, K. (1991). Structure and function of myelin protein genes. Annu. Rev. Neurosci. *14*, 201–217.

Nori, S., Okada, Y., Yasuda, A., Tsuji, O., Takahashi, Y., Kobayashi, Y., Fujiyoshi, K., Koike, M., Uchiyama, Y., Ikeda, E., et al. (2011). Grafted human-induced pluripotent stem-cell-derived neurospheres promote motor functional recovery after spinal cord injury in mice. Proc. Natl. Acad. Sci. USA *108*, 16825–16830.

Ohta, S., Imaizumi, Y., Okada, Y., Akamatsu, W., Kuwahara, R., Ohyama, M., Amagai, M., Matsuzaki, Y., Yamanaka, S., Okano, H., and Kawakami, Y. (2011). Generation of human melanocytes from induced pluripotent stem cells. PLoS ONE *6*, e16182.

Okada, Y., Shimazaki, T., Sobue, G., and Okano, H. (2004). Retinoic-acid-concentration-dependent acquisition of neural cell identity during in vitro differentiation of mouse embryonic stem cells. Dev. Biol. *275*, 124–142.

Okada, Y., Matsumoto, A., Shimazaki, T., Enoki, R., Koizumi, A., Ishii, S., Itoyama, Y., Sobue, G., and Okano, H. (2008). Spatiotemporal recapitulation of central nervous system development by murine embryonic stem cell-derived neural stem/progenitor cells. Stem Cells *26*, 3086–3098.

Seitelberger, F. (1995). Neuropathology and genetics of Pelizaeus-Merzbacher disease. Brain Pathol. *5*, 267–273.

Shimada, H., Okada, Y., Ibata, K., Ebise, H., Ota, S., Tomioka, I., Nomura, T., Maeda, T., Kohda, K., Yuzaki, M., et al. (2012). Efficient derivation of multipotent neural stem/progenitor cells from non-human primate embryonic stem cells. PLoS ONE *7*, e49469.

Shimojima, K., Inoue, T., Imai, Y., Arai, Y., Komoike, Y., Sugawara, M., Fujita, T., Ideguchi, H., Yasumoto, S., Kanno, H., et al. (2012). Reduced PLP1 expression in induced pluripotent stem cells derived from a Pelizaeus-Merzbacher disease patient with a partial PLP1 duplication. J. Hum. Genet. *57*, 580–586.

Southwood, C.M., Garbern, J., Jiang, W., and Gow, A. (2002). The unfolded protein response modulates disease severity in Pelizaeus-Merzbacher disease. Neuron *36*, 585–596.

Takahashi, K., Tanabe, K., Ohnuki, M., Narita, M., Ichisaka, T., Tomoda, K., and Yamanaka, S. (2007). Induction of pluripotent stem cells from adult human fibroblasts by defined factors. Cell *131*, 861–872.

Thomson, C.E., Montague, P., Jung, M., Nave, K.A., and Griffiths, I.R. (1997). Phenotypic severity of murine Plp mutants reflects in vivo and in vitro variations in transport of PLP isoproteins. Glia *20*, 322–332.

Wang, S., Bates, J., Li, X., Schanz, S., Chandler-Militello, D., Levine, C., Maherali, N., Studer, L., Hochedlinger, K., Windrem, M., and Goldman, S.A. (2013). Human iPSC-derived oligodendrocyte progenitor cells can myelinate and rescue a mouse model of congenital hypomyelination. Cell Stem Cell *12*, 252–264.

Yin, X., Baek, R.C., Kirschner, D.A., Peterson, A., Fujii, Y., Nave, K.A., Macklin, W.B., and Trapp, B.D. (2006). Evolution of a neuroprotective function of central nervous system myelin. J. Cell Biol. *172*, 469–478.

nature COMMUNICATIONS

ARTICLE

Received 12 May 2014 | Accepted 8 Oct 2014 | Published 24 Nov 2014

DOI: 10.1038/ncomms6514

OPEN

Pathological roles of the VEGF/SphK pathway in Niemann-Pick type C neurons

Hyun Lee[1,2,*], Jong Kil Lee[1,3,4,*], Min Hee Park[1,3,4], Yu Ri Hong[1,2], Hugo H. Marti[5], Hyongbum Kim[6], Yohei Okada[7], Makoto Otsu[8], Eul-Ju Seo[9], Jae-Hyung Park[10], Jae-Hoon Bae[10], Nozomu Okino[11], Xingxuan He[12], Edward H. Schuchman[12], Jae-sung Bae[1,3,4] & Hee Kyung Jin[1,2]

Sphingosine is a major storage compound in Niemann-Pick type C disease (NP-C), although the pathological role(s) of this accumulation have not been fully characterized. Here we found that sphingosine kinase (SphK) activity is reduced in NP-C patient fibroblasts and NP-C mouse Purkinje neurons (PNs) due to defective vascular endothelial growth factor (VEGF) levels. Sphingosine accumulation due to inactivation of VEGF/SphK pathway led to PNs loss via inhibition of autophagosome-lysosome fusion in NP-C mice. VEGF activates SphK by binding to VEGFR2, resulting in decreased sphingosine storage as well as improved PNs survival and clinical outcomes in NP-C cells and mice. We also show that induced pluripotent stem cell (iPSC)-derived human NP-C neurons are generated and the abnormalities caused by VEGF/SphK inactivity in these cells are corrected by replenishment of VEGF. Overall, these results reveal a pathogenic mechanism in NP-C neurons where defective SphK activity is due to impaired VEGF levels.

---

[1] Stem Cell Neuroplasticity Research Group, Kyungpook National University, Daegu 702-701, Korea. [2] Department of Laboratory Animal Medicine, Cell and Matrix Research Institute, College of Veterinary Medicine, Kyungpook National University, Daegu 702-701, Korea. [3] Department of Physiology, Cell and Matrix Research Institute, School of Medicine, Kyungpook National University, Daegu 700-842, Korea. [4] Department of Biomedical Science, BK21 Plus KNU Biomedical Convergence Program, Kyungpook National University, Daegu 700-842, Korea. [5] Institute of Physiology and Pathophysiology, University of Heidelberg, Heidelberg 69120, Germany. [6] Graduate School of Biomedical Science and Engineering/College of Medicine, Hanyang University, Seoul 133-791, Korea. [7] Department of Physiology, School of Medicine, Keio University, Tokyo 160-8582, Japan. [8] Division of Stem Cell Therapy, Center for Stem Cell Biology and Regenerative Medicine, Institute of Medical Science, University of Tokyo, Tokyo 108-8639, Japan. [9] Department of Laboratory Medicine, Asan Medical Center, University of Ulsan College of Medicine, Seoul 138-736, Korea. [10] Department of Physiology, School of Medicine, Keimyung University, Daegu 704-701, Korea. [11] Department of Bioscience and Biotechnology, Graduate School of Bioresource and Bioenvironmental Sciences, Kyushu University, Fukuoka 812-8581, Japan. [12] Department of Genetics and Genomic Sciences, Icahn School of Medicine at Mount Sinai, New York, New York 10029, USA. * These authors contributed equally to this work. Correspondence and requests for materials should be addressed to J.S.B. (email: jsbae@knu.ac.kr) or to H.K.J. (email: hkjin@knu.ac.kr).

Niemann-Pick type C disease (NP–C) is an inherited lipid storage disorder that affects the central nervous system[1–3]. Recent studies have shown that sphingosine is a major and initiating storage compound in NP–C[3,4]. However, the underlying mechanism(s) leading to sphingosine storage, as well as its role in NP–C pathogenesis such as neuronal loss, remains largely unknown.

Our previous studies have shown that bone marrow mesenchymal stem cells (BM-MSCs) contribute to improved neurological function in the NP–C mice[5,6]. Furthermore, we have postulated that the prosurvival effects of BM-MSCs on NP–C Purkinje neurons (PNs) are paracrine effects that restore the sphingolipid imbalance, as evidenced by decreased sphingosine and increased sphingosine-1-phosphate (S1P) levels[7]. Therefore, we speculated that sphingolipid-modulating factors derived from BM-MSCs are potential therapeutic agents for this disease.

Sphingolipid-metabolizing enzymes control the cellular dynamic balance of bioactive lipids, including the proapoptotic compound sphingosine and the proliferative compound S1P[8]. Sphingosine kinase (SphK) is a key enzyme that converts sphingosine into S1P. SphK can be activated by numerous external stimuli[9–12], resulting in a decrease in intracellular sphingosine and increase in S1P[13].

On the basis of these concepts and findings, we hypothesized that defects of SphK activators could be involved in the pathogenesis of NP–C, and explored candidate therapeutic factors secreted by BM-MSCs that might influence the activation of SphK. Here we show that NPC1 deficiency markedly reduces vascular endothelial growth factor (VEGF) expression, and that decreased VEGF levels cause impaired SphK activity in PNs. Abnormal sphingosine storage by VEGF-mediated SphK inactivity causes a decreased PN survival via disruption of autophagosome–lysosome fusion. Further, replenishment of VEGF leads to restoration of SphK activity and improvement of pathology by binding to the VEGF receptor-2 (VEGFR2) in NP–C mice PNs as well as patient-specific cells, preventing sphingosine accumulation, autophagy dysfunction and abnormal calcium homeostasis.

Results

SphK activity is reduced in NP–C patients and NP–C mice. We first determined whether defects of SphK could be involved in NP–C and responsible for the elevated sphingosine. SphK was significantly decreased in fibroblasts from NP–C patients compared with normal control fibroblasts (Fig. 1a). These levels did not change as the passage numbers increased (Fig. 1a). SphK activity also was decreased in the cerebellum and primary cerebellar PNs from NP–C mice compared with those of wild-type (WT) mice (Fig. 1a). These results confirmed that SphK, a key enzyme in modulating the levels of sphingosine, is diminished in NP–C, and that the reduction of this activity may influence disease progression and/or pathogenesis.

BM-MSC-derived VEGF restores SphK activity in NP–C mouse PNs. To examine whether bioactive, soluble factors released from BM-MSCs affected SphK activity in NP–C, we cocultured BM-MSCs with PNs using an indirect coculture system (see Methods). We found that when NP–C PNs were cocultured with BM-MSCs, their SphK activity was significantly increased (Fig. 1b). To identify the soluble factors that were released from the BM-MSCs and might be responsible for the increased SphK activity, we screened and compared the conditioned media (CM) of PNs grown with and without BM-MSCs using an antibody-based mouse cytokine array (Supplementary Fig. 1a,b). The CM of NP–C PNs cocultured with BM-MSCs revealed stronger signals in four array spots in comparison with the CM of NP–C PNs alone (Supplementary Fig. 1c,d). To confirm the secretion of these factors, we performed enzyme-linked immunosorbent assays (ELISA). Of the selected cytokines, only VEGF levels were significantly elevated in the CM of NP–C PNs cocultured with BM-MSCs. We also found that VEGF was significantly decreased in NP–C PNs cultured alone compared with WT PNs (Fig. 1c). To confirm these effects in PNs, we performed VEGF immunostaining. VEGF was normally expressed in PNs, but the expression levels were lower in NP–C PNs compared with WT PNs. When the NP–C PNs were cocultured with BM-MSCs, intensity of VEGF expression was increased (Fig. 1d). These data identified VEGF as a potential candidate molecule that could modulate SphK and may influence pathogenesis in NP–C PNs.

To further examine the effects of BM-MSC-derived VEGF on SphK activity in NP–C PNs, we used VEGF small interfering RNA (siRNA)-treated BM-MSCs and VEGF-overexpressing BM-MSCs (the latter derived from VEGF^{tg} mice; ref. 14; Supplementary Fig. 2a). As predicted, SphK activity was significantly increased in NP–C PNs cocultured with BM-MSCs and VEGF^{tg} BM-MSCs compared with NP–C PNs alone. However, the activity did not show any changes in NP–C PNs cocultured with VEGF siRNA-treated BM-MSCs (Fig. 1e). Consistent with this observation, sphingosine and S1P levels in the cocultured NP–C PNs were altered relative to the amount of VEGF released from the BM-MSCs (Supplementary Fig. 2b,c). We also performed S1P immunostaining in PNs. S1P was mainly expressed in PNs, and the expression was significantly increased in NP–C PNs cocultured with normal or VEGF^{tg} BM-MSCs. However, it was not increased when the cells were cocultured with VEGF siRNA-treated BM-MSCs (Supplementary Fig. 2d).

VEGF binds to two tyrosine kinase receptors, known as VEGFR1 and 2 (ref. 15). Among these receptors, VEGFR2 is highly expressed on PNs[16]. To examine whether VEGF from BM-MSCs improved the sphingolipid imbalance in NP–C PNs by binding to VEGFR2, we treated NP–C PNs with the VEGFR2 tyrosine kinase inhibitor PTK787 before coculturing[17]. We found that SphK activity and other sphingolipid metabolites in NP–C PNs were mediated by interactions of BM-MSC-derived VEGF and its receptor VEGFR2 (Fig. 1f; Supplementary Fig. 2e). These results indicated that BM-MSC-mediated restoration of abnormal SphK activity could be due the secreted VEGF binding to the VEGFR2 in NP–C PNs.

Next, to determine whether the VEGF-mediated SphK modulation by BM-MSCs promoted the survival of NP–C PNs, we determined cell counts after coculture. When NP–C PNs were cocultured with BM-MSCs or VEGF^{tg} BM-MSCs, the number of PNs was significantly increased. This effect was lower when VEGF siRNA BM-MSCs were cocultured with the NP–C PNs, although this did not reach statistical significance (Fig. 1g).

Finally, to gain more direct insights into the relationship between VEGF and SphK activity in NP–C PNs, we treated WT PNs with VEGF siRNA and determined the changes of sphingolipid factors. VEGF siRNA treatment of WT PNs strongly reduced SphK levels and led to elevation of sphingosine and reduction of S1P, similar to NP–C PNs (Fig. 1h; Supplementary Fig. 2f,g). The survival of PNs was also significantly decreased following VEGF siRNA transfection (Fig. 1i). These results suggested that inactivation of VEGF may lead to reduced SphK activity in NP–C PNs.

VEGF from BM-MSCs reduces pathology in PNs of NP–C mice. To examine the *in vivo* effects of VEGF derived from BM-MSCs on SphK activity of PNs, we transplanted BM-MSCs into the cerebellum of NP–C mice (Fig. 2a). At one day after BM-MSC

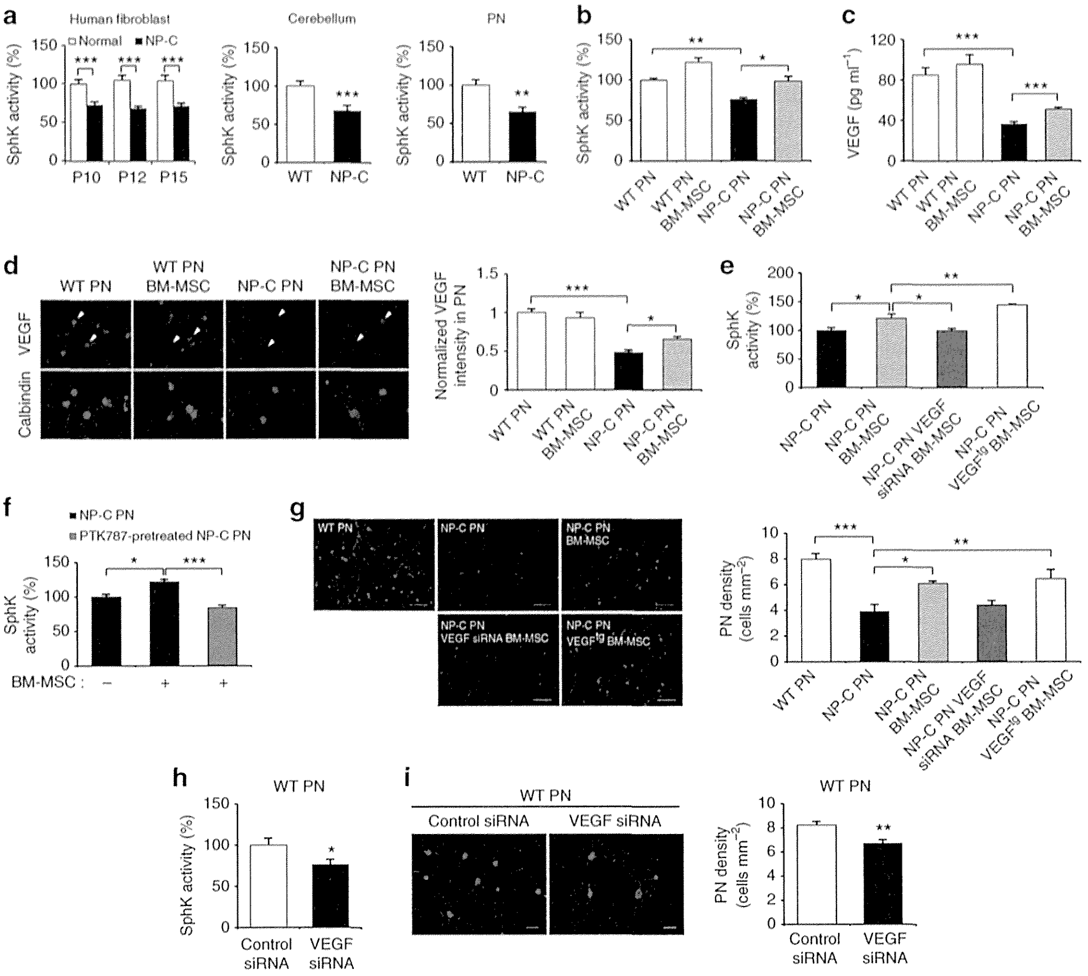

Figure 1 | BM-MSC-derived VEGF restores SphK activity in NP-C mice PNs. (**a**) SphK activities between NP-C and control were analysed in human fibroblast ($n=7$ per group), mouse cerebellum tissue ($n=7$ per group) and primary mouse PN samples ($n=9$ per group). SphK activity did not show passage differences between NP-C and normal fibroblasts. (**b**) Three days after cocultures, we measured SphK activities in PNs derived from WT and NP-C mice ($n=8$ per group). (**c**) VEGF levels were measured in CM derived from PNs with or without BM-MSCs by ELISA ($n=7$ per group). (**d**) Primary cultures of NP-C PNs were immunostained with anti-calbindin and anti-VEGF (scale bar, 50 μm). Arrowheads indicate VEGF expression by PNs. Values represent normalized fluorescence intensities of VEGF in PNs (WT PN, $n=8$; and NP-C PN, $n=9$). (**e**) SphK activities were measured in NP-C PNs alone ($n=7$) and NP-C PNs cocultured with BM-MSCs, VEGF siRNA BM-MSCs and VEGF^{tg} BM-MSCs ($n=8$ per group). (**f**) Effect of the PTK787 on BM-MSCs mediated SphK activation. NP-C PNs were pretreated with PTK787 at 10 μM for 1 day and cocultured for 3 days with BM-MSCs, and then SphK activity was assayed ($n=7$ per group). (**g**) Representative images of PNs stained with anti-calbindin (scale bar, 100 μm). The mean number of PNs per squared millimetre was counted ($n=8$ per group). (**h**) Effect of VEGF knockdown on SphK activity in PNs (control, $n=6$; and VEGF siRNA, $n=8$ per group). (**i**) Representative images and quantification of neuronal survival in normal and VEGF-knockdown PNs (scale bar, 50 μm; $n=8$ per group). **a**,**h**,**i**, Student's *t*-test. **b-g**, one-way analysis of variance, Tukey's *post hoc* test. $^*P<0.05$, $^{**}P<0.01$, $^{***}P<0.005$. All error bars indicate s.e.m.

transplantation, SphK activity was significantly increased in the cerebellum of NP–C mice compared with phosphate-buffered saline (PBS)-infused counterparts (Fig. 2b). BM-MSC transplantation also increased VEGF protein levels in the cerebellum of NP–C mice (Fig. 2c). The elevated expression of VEGF was significant in the Purkinje cell layer (PCL) of the NP–C mouse cerebellums, consistent with the decreased VEGF levels in non-treated NP–C PNs compared with WT (Fig. 2d). However, BM-MSCs did not increase SphK or VEGF levels in normal cerebellums, consistent with previous reports[6,18].

We also transplanted VEGF siRNA BM-MSCs and VEGF^{tg} BM-MSCs into the cerebellum of NP–C mice. As predicted, at one day after transplantation, SphK activity was significantly increased in the cerebellum of NP–C mice treated with VEGF^{tg} BM-MSCs. However, mice treated with VEGF siRNA BM-MSCs showed significantly lower SphK activity (Fig. 2e). The sphingosine and S1P metabolites were also changed in NP–C PNs in relation to SphK and VEGF levels (Supplementary Fig. 3a,b). Similar effects were observed when S1P immunostaining was performed on the PN layer of NP–C mice following transplantation with VEGF siRNA or VEGF-overexpressing BM-MSCs (Supplementary Fig. 3c). To further confirm these effects, we used laser capture microdissection (LCM) to selectively isolate PNs (Supplementary Fig. 3d). We observed that expressions of *Vegf*, *VEGFR2* and *Sphk1* mRNAs were decreased in LCM-captured PNs from NP–C mice compared with that of WT mice. BM-MSC transplantation enhanced these expression levels in NP–C PNs (Fig. 2f). We also ascertained whether VEGFR2 was required for the activation of SphK in NP–C mice. As shown in Fig. 2g, SphK activity was significantly increased in the NP–C mice following BM-MSC treatment, whereas this effect was lower in NP–C mice treated with PTK787 before injecting BM-MSCs,

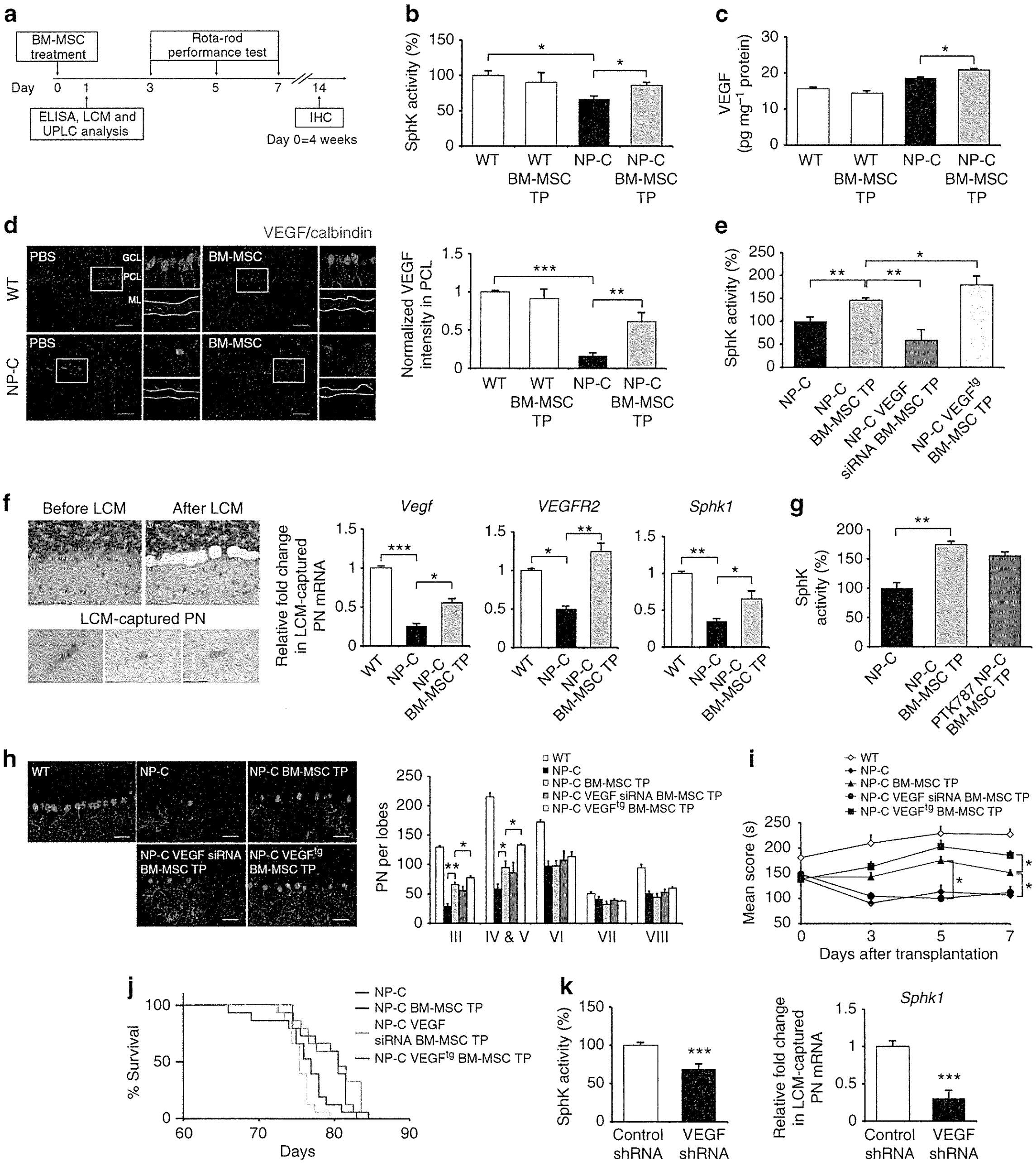

Figure 2 | VEGF from BM-MSCs reduces pathology in PNs of NP-C mice. (**a**) Protocol of BM-MSC treatment in NP-C mice. (**b**,**c**) SphK activity ($n=7$ per group; **b**) and VEGF levels ($n=8$ per group; **c**) were estimated in the cerebellums of WT and NP-C mice after BM-MSC treatment. (**d**) Cerebellar sections were stained with anti-calbindin and anti-VEGF (low-magnification scale bar, 50 μm; high-magnification scale bar, 20 μm). Values represent normalized VEGF fluorescence intensities in PCL ($n=7$ per group). (**e**) SphK activities were measured in the cerebellums of NP-C mice treated with PBS ($n=6$), BM-MSCs, VEGF siRNA BM-MSCs and VEGF^{tg} BM-MSCs ($n=8$ per group). (**f**) Left, isolation of mouse PNs using LCM (scale bar, 75 μm). Right, mRNA level of *Vegf*, *VEGFR2* and *Sphk1* on LCM-captured PNs samples ($n=7$ per group). (**g**) NP-C mice were treated daily with the PTK787 at 100 mg kg^{-1} or PBS, starting 2 days before the BM-MSC transplantation. One day after BM-MSC treatment, SphK activity was estimated (NP-C, $n=7$; NP-C BM-MSC TP, $n=8$ per group). (**h**) Cerebellar sections were stained with anti-calbindin (scale bar, 50 μm), and the number of calbindin-positive PNs were quantified ($n=7$ per group). (**i**) Rota-rod scores of mice were averaged and plotted beginning 3 days after transplantation ($n=15$ per group). (**j**) Survival curve of NP-C mice ($n=15$ per group). Treatment with BM-MSCs and VEGF^{tg} BM-MSCs resulted in significantly increased survival compared with PBS treatment ($P=0.0194$ and $P=0.0055$, respectively; log-rank test). (**k**) Effect of VEGF knockdown on SphK activity. Left, after intracerebellar injection of control ($n=7$) or VEGF shRNA ($n=8$) in mice, SphK activities were measured in the cerebellums. Right, relative levels of *Sphk1* mRNA from LCM-captured PNs samples ($n=7$ per group). **b**-**i**, one-way analysis of variance, Tukey's *post hoc* test. **k**, Student's *t*-test. $^{*}P<0.05$, $^{**}P<0.01$, $^{***}P<0.005$. All error bars indicate s.e.m.

although this did not reach statistical significance. S1P levels were moderately decreased with PTK787 treatment, but sphingosine did not vary between the groups (Supplementary Fig. 3e).

Next, we evaluated the effects of VEGF on the NP–C phenotype in mice. Transplantation of VEGF^{tg} BM-MSCs improved NP–C pathology as measured by increased number of calbindin-positive PNs on 14 days after treatment (Fig. 2h), and also enhanced the Rota-rod performance (Fig. 2i). These effects were less in the VEGF siRNA BM-MSC-treated group. Rota-rod performance also diminished in the VEGF siRNA BM-MSC-treated NP–C mice over time. Moreover, the lifespan of mice that had BM-MSC or VEGF^{tg} BM-MSC transplants was extended (Fig. 2j).

Finally, to determine whether the reduced VEGF levels in the cerebellums affected SphK activity, we injected VEGF short hairpin RNA (shRNA) into the cerebellum of WT mice and determined the changes of sphingolipid factors. Treatment with VEGF shRNA markedly reduced SphK activity and *Sphk1* mRNA levels (Fig. 2k; Supplementary Fig. 3f,g) and led to elevation of sphingosine and reduction of S1P (Supplementary Fig. 3h). These results suggested that inactivation of VEGF may lead to reduced SphK activity in NP–C mice, consistent with *in vitro* results. Together, these findings show a direct correlation between VEGF and SphK activity in PNs and suggest that abnormal sphingosine accumulation in NP–C may be due to the dysfunction of SphK activity by inactivated VEGF expression.

NPC1 deficiency impairs VEGF/SphK activation in PNs. We subsequently investigated the relationship between NPC1 and VEGF expression. NPC1 knockdown by siRNA markedly decreased VEGF expression in normal PNs. When NPC1 was knocked down in VEGF^{tg} PNs (derived from VEGF^{tg} mice), the decreased level of VEGF was lower than that of normal PNs (Fig. 3a–c). Moreover, NPC1 deficiency markedly inactivated SphK and led to sphingolipid imbalance. In VEGF^{tg} PNs, however, moderate changes were observed (Fig. 3d,e). We next tested whether NPC1 deficiency affected VEGF expression in the

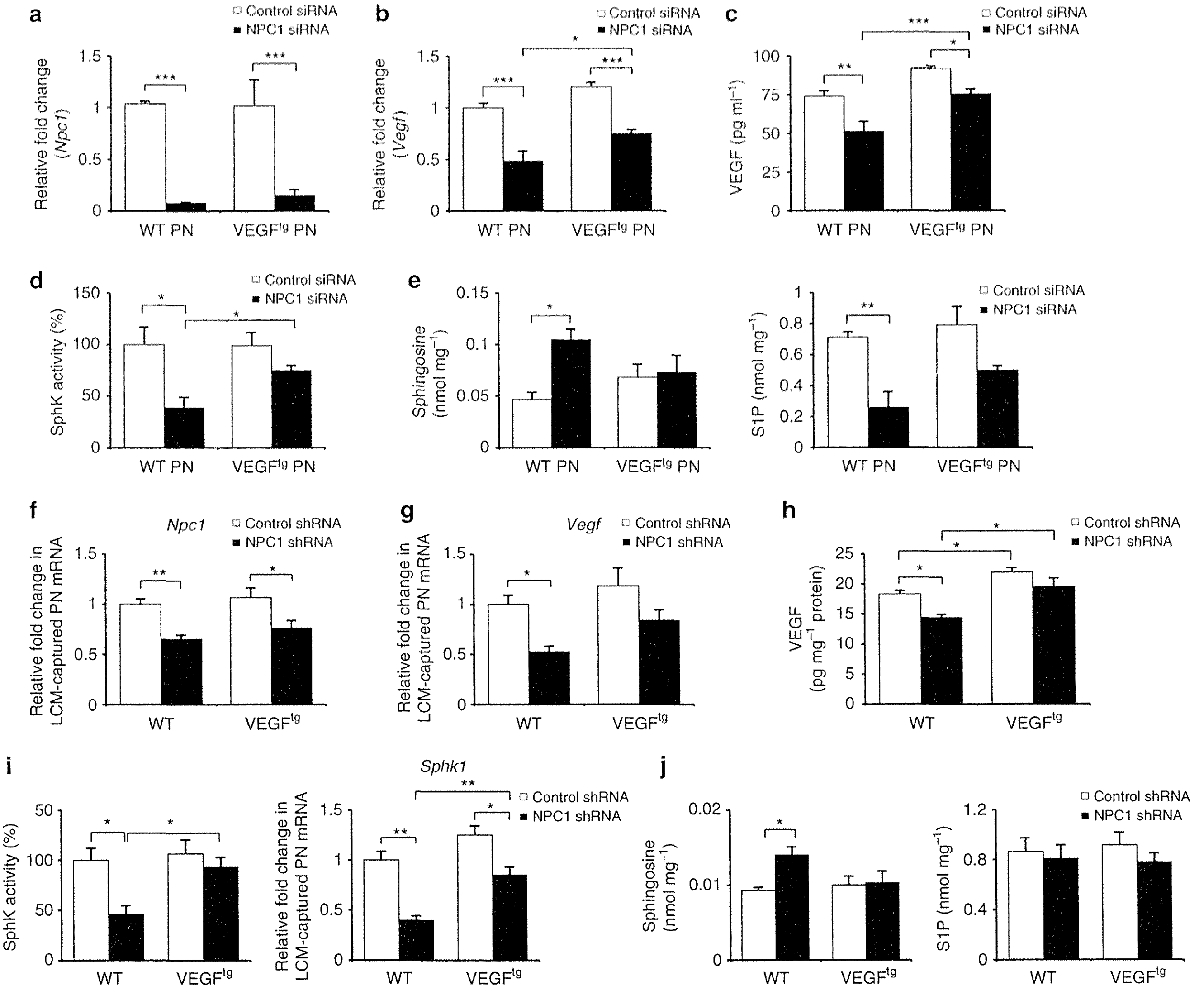

Figure 3 | NPC1 knockdown reduces VEGF expression and SphK activity. (**a–c**) Primary cultures of normal and VEGF^{tg} PNs were transfected with control or NPC1 siRNA. Three days after transfection, we measured the levels of *Npc1* (**a**) and *Vegf* (**b**) mRNA and secreted VEGF protein (**c**) in PNs ($n = 7$ per group). (**d**,**e**) SphK activity (**d**), sphingosine and S1P (**e**) were estimated in PNs transfected with control ($n = 6$) or NPC1 siRNA ($n = 7$). (**f–j**) Four-week-old WT and VEGF^{tg} mice were injected with control or NPC1 shRNA into the cerebellum. Mice were sacrificed at 3 days after the injection. *Npc1* (**f**) and *Vegf* (**g**) mRNA levels were estimated in LCM-captured PNs and VEGF protein levels (**h**) were measured in the cerebellums ($n = 7$ per group). (**i**) Left, SphK activities were measured in the cerebellums ($n = 7$ per group). Right, relative levels of *Sphk1* mRNA from LCM-captured PNs samples ($n = 8$ per group). (**j**) Sphingosine and S1P were measured in the cerebellums ($n = 7$ per group). **a–j**, one-way analysis of variance, Tukey's *post hoc* test. $^{*}P < 0.05$, $^{**}P < 0.01$, $^{***}P < 0.005$. All error bars indicate s.e.m.

cerebellums of WT mice using NPC1 shRNA. Intracerebellar injection of NPC1 shRNA, which decreased *Npc1* mRNA expression in the LCM-captured PNs (Fig. 3f), reduced VEGF expression (Fig. 3g,h). Consistently, NPC1 deficiency significantly decreased SphK activity and *Sphk1* mRNA expression and led to elevation of sphingosine and reduction of S1P in the cerebellums (Fig. 3i,j). These effects were moderated in VEGF^{tg} mice (Fig. 3g–j). Overall, these results indicated that knockdown of NPC1 may lead to reduced VEGF expression, and these reductions subsequently decreased SphK activity in PNs.

VEGF overexpression ameliorates NP-C pathology in mice. The VEGF-mediated SphK reduction in NP-C PNs prompted us to examine possible genetic implications of this pathway. To increase VEGF in NP-C mice, we generated *VEGF*^{tg}/*Npc1*$^{-/-}$ mice (Supplementary Fig. 4a). VEGF is widely expressed in neurons, glia and endothelial cells[19,20], with strong expression in PNs. In NP-C cerebellum, however, VEGF was mainly expressed in the granular layer and significantly decreased in the PCL. VEGF/NP-C mice showed increased expression of VEGF in the PCL compared with NP-C mice (Fig. 4a).

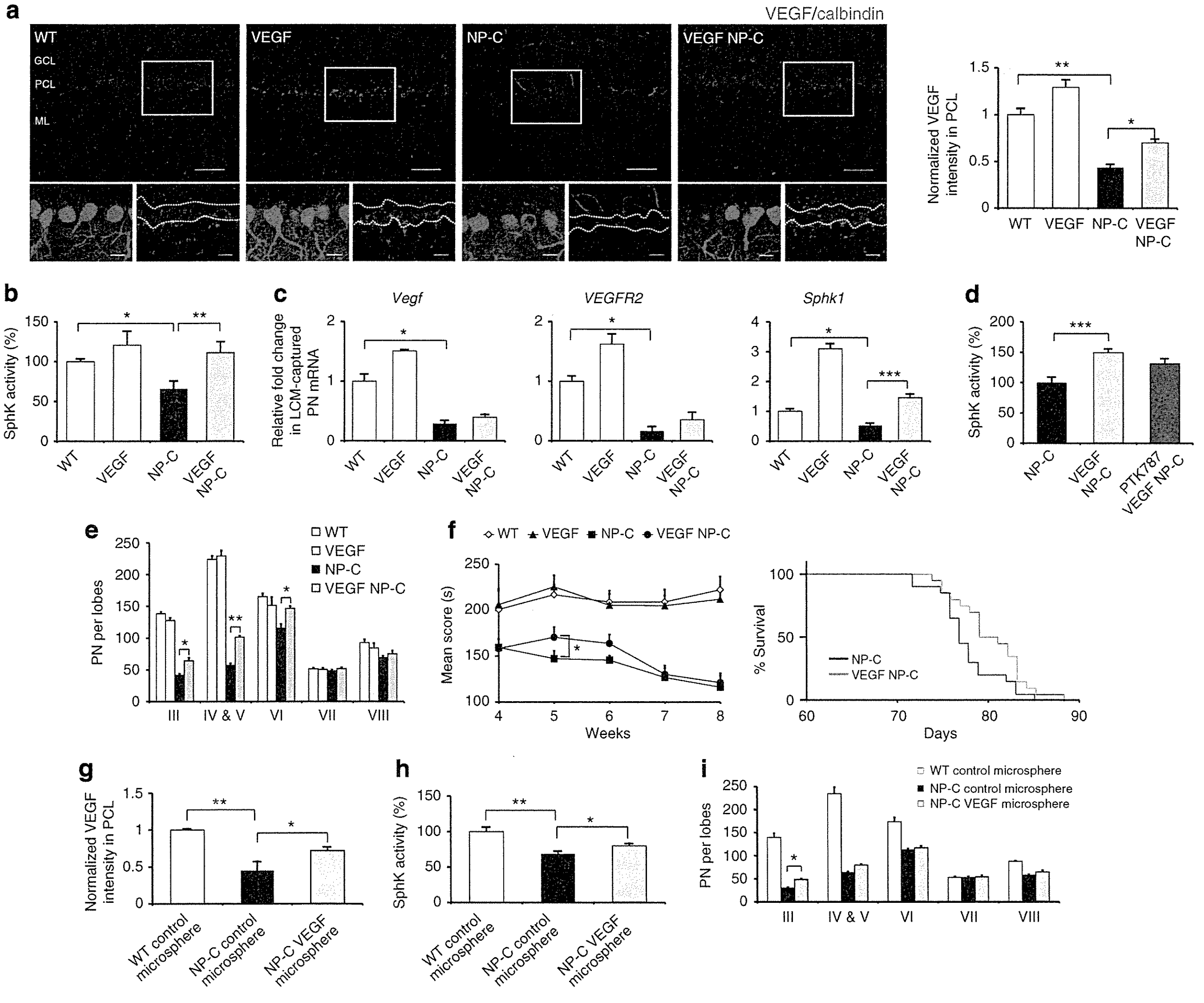

Figure 4 | Replenishment of VEGF ameliorates NP-C pathology in mice. (**a**) Cerebellar sections from 6-week-old WT, VEGF, NP-C and VEGF/NP-C mice were immunostained with anti-calbindin and anti-VEGF (low-magnification scale bar, 50 μm; high-magnification scale bar, 20 μm). The average VEGF fluorescence intensity within the PCL was measured (WT, $n=7$; VEGF, $n=7$; NP-C, $n=9$; and VEGF/NP-C, $n=9$). (**b**) SphK activities were measured in cerebellums derived from 6-week-old WT, VEGF, NP-C and VEGF/NP-C mice ($n=8$ per group). (**c**) Quantitative real-time PCR for *Vegf*, *VEGFR2* and *Sphk1* mRNA in LCM-captured PNs in 6-week-old WT, VEGF, NP-C and VEGF/NP-C mice (WT, $n=6$; VEGF, $n=6$; NP-C, $n=8$; and VEGF/NP-C, $n=8$). (**d**) VEGF/NP-C mice were treated daily with the PTK787 at 100 mg kg^{-1} or PBS vehicle control for 3 days before sacrifice (6-week-old), and SphK activity was estimated in cerebellums ($n=7$ per group). (**e**) Cerebellar sections were immunostained with anti-calbindin and the number of calbindin-positive PNs was quantified (WT, $n=7$; VEGF, $n=7$; NP-C, $n=8$; and VEGF/NP-C, $n=8$). (**f**) Left, beginning at 4 weeks of age, Rota-rod scores were averaged and plotted ($n=15$ per group). Right, survival curves of NP-C and VEGF/NP-C mice ($P=0.0548$; log-rank test, $n=15$ per group). (**g**) Cerebellar sections from WT and NP-C mice transplanted with VEGF-loaded or control microspheres were stained with anti-calbindin and anti-VEGF. The average VEGF fluorescence intensity within the PCL was measured ($n=7$ per group). (**h**) SphK activity was estimated in the cerebellums of WT and NP-C mice at one day after treatment. (**i**) Cerebellar sections were prepared at 2 weeks after transplantation and immunostained with anti-calbindin. The calbindin-positive PNs were counted ($n=7$ per group). **a**-**i**, one-way analysis of variance, Tukey's *post hoc* test. $^{*}P<0.05$, $^{**}P<0.01$, $^{***}P<0.005$. All error bars indicate s.e.m.

To examine whether genetically increasing VEGF affects SphK activity in NP–C PNs, we analysed cerebellum samples derived from 6-week-old WT, VEGF, NP–C and VEGF/NP–C mice. Compared with NP–C mice, VEGF/NP–C mice showed significantly increased SphK activity and decreased sphingosine accumulation (Fig. 4b; Supplementary Fig. 4b). Cerebellar S1P levels did not vary between the NP–C and VEGF/NP–C mice, although S1P levels in the PCL was increased in VEGF/NP–C mice (Supplementary Fig. 4b,d). Sphingomyelin and unesterified cholesterol levels were also significantly decreased in VEGF/NP–C mice, but glycosphingolipid (GSL) levels did not vary between the groups (Supplementary Fig. 4c,e,f). These results revealed that genetic VEGF overexpression could reverse the SphK abnormality and abnormal lipid accumulation in NP–C. To confirm VEGF-mediated SphK activation within PNs, we measured the *Vegf*, *VEGFR2* and *Sphk1* mRNA levels in LCM-captured PNs from these mice. LCM-captured PNs from VEGF/NP–C showed slightly increased *Vegf* and *VEGFR2* mRNA levels and significantly enhanced *Sphk1* mRNA levels (Fig. 4c).

Next, to further investigate the subcellular distribution pattern of SphK activity, sphingosine and S1P, we isolated cytosolic-enriched and lysosome-enriched fractions from the cerebellums. SphK activity was increased in VEGF/NP–C-derived lysosomes and cytosol compared with NP–C-derived ones, although the degree of SphK increase was greater in the cytosol than lysosome. Accumulated sphingosine in NP–C was found in the lysosome. Lysosomal sphingosine levels were significantly decreased in the VEGF/NP–C, whereas S1P levels did not vary between the groups (Supplementary Fig. 4g). Taken together, these results suggested that VEGF leads to activated SphK in the lysosome and cytosol and that activated SphK decreased lysosomal sphingosine accumulation in NP–C. We next observed whether the activation of VEGFR2 was required for the activation of SphK in VEGF/NP–C mice. Increased SphK activity was lower in VEGF/NP–C mice treated with the PTK787, although this did not reach statistical significance (Fig. 4d). Sphingosine levels also were moderately increased, but S1P levels did not vary between the groups (Supplementary Fig. 4h). PN survival was significantly improved in the VEGF/NP–C mice (Fig. 4e), and there were improvements in the Rota-rod score of 5-week-old VEGF/NP–C mice compared with NP–C mice (Fig. 4f, left). The lifespan of the VEGF/NP–C mice was slightly increased (Fig. 4f, right). We also found that BM-MSC transplantation is more effective in SphK modulation than genetic replenishment of VEGF (see Fig. 2). These results suggested that other factors secreted by BM-MSCs might also contribute to SphK activation.

We next tested whether pharmacologic delivery of recombinant VEGF is beneficial to NP–C pathology. Since the injected recombinant VEGF exerted a short-lived effect[21], to overcome this obstacle we generated a microsphere system that allows localized and sustained VEGF release (Supplementary Fig. 5a). We injected 3 mg of VEGF-loaded microspheres or control microspheres into the cerebellum of 4-week-old NP–C and WT mice. Two weeks after treatment, NP–C mice transplanted with VEGF-loaded microspheres had higher levels of VEGF expression in the PCLs (Fig. 4g), exhibited increased SphK activity (Fig. 4h) and decreased sphingosine levels (Supplementary Fig. 5b) in their cerebellums. S1P levels in cerebellum and expression in PNs were also increased by VEGF-loaded microsphere treatment (Supplementary Fig. 5b,c). Further, the VEGF-loaded microsphere-treated NP–C mice showed significantly improved PN survival (Fig. 4i).

VEGF overexpression reverses defective autophagy in NP–C mice. Autophagy, a major degradative pathway of the lysosomal system, is known to be markedly impaired in NP–C. These defects lead to loss of PNs in NP–C[22]. To examine whether increased PN survival in VEGF/NP–C mice was related to autophagy, we first measured LC3-II levels. Consistent with previous result[22], we found that the LC3-II levels were significantly increased in PNs and cerebellum samples derived from NP–C mice. This enhanced LC3-II level was reduced in VEGF/NP–C mice (Fig. 5a,b,d). The level of beclin-1 did not vary between the groups (Fig. 5a,d). The levels of cathepsin D, a lysosomal hydrolase, were slightly increased in NP–C mice compared with WT mice (Fig. 5a,d). However, the activity of cathepsin D was not changed between the groups (Fig. 5c,e). This result indicated that the elevated levels of cathepsin D in NP–C mice did not ultimately translate into a significant increase in enzyme activity. Cathepsin D levels in VEGF/NP–C mice were comparable to that of NP–C mice, indicating that increased VEGF in NP–C mice did not influence the cathepsin D expression (Fig. 5a,c–e). The level of p62 was significantly higher in NP–C mice compared with WT mice, but was decreased in VEGF/NP–C mice (Fig. 5a,d). We also performed transmission electron microscopic (EM) analysis using mouse cerebellum samples to corroborate the immunoblotting results. NP–C mice brains showed massive increases of autophagic vacuoles, while brains of VEGF/NP–C mice represented a reduced number of these vesicles (Fig. 5f).

Next, to determine whether the endocytic pathway was affected by VEGF overexpression in NP–C mice, we examined Rab5 and Rab7 expression in our animals. The levels of these proteins showed no differences between the groups (Fig. 5g). Apoptotic cells, as judged by active caspase-3, did not show any differences between NP–C and VEGF/NP–C mice (Fig. 5h). Our results showed that endocytic pathway and apoptosis were not the main mechanisms of increased PN survival in VEGF/NP–C mice.

Impaired VEGF/SphK pathway causes defective autophagic flux. Improved autophagic degradation in the VEGF/NP–C mice prompted us to analyze whether VEGF-mediated sphingolipid changes affect autophagy activity. First, to unravel the mechanistic link between VEGF levels and autophagic dysfunction, VEGF was depleted in the WT PNs by siRNA treatment. Knockdown of VEGF caused increased accumulation of LC3-II and p62 (Fig. 6a,b). Beclin-1 expression was not affected by VEGF knockdown (Fig. 6a), indicating that the accumulation of autophagosomes was not due to the biogenesis pathway.

The accumulation of autophagosomes can occur due to either an increase in their rate of formation or a reduction in their rate of degradation[23]. To distinguish between these two events, we examined the effects of VEGF knockdown on LC3-II levels in WT PNs in the presence or absence of NH_4Cl that blocks autophagic degradation but does not affect autophagosome formation. VEGF knockdown increased accumulation of LC3-II. This level was not further increased by NH_4Cl treatment (Fig. 6c, left). In contrast, VEGF depletion in serum starvation culture resulted in a significant increase in LC3-II levels (Fig. 6c, right). These observations were also supported by levels of p62 (Fig. 6c). These results suggested that VEGF depletion influences at a late step of autophagy. We also performed autophagy flux assay in WT, NP–C and VEGF/NP–C mice PNs. Under basal condition, NP–C PNs showed significantly increased LC3-II and p62 levels compared with WT PNs. NH_4Cl-induced lysosome inhibition led to marked increase of LC3-II and p62 levels in the WT PNs, but this increase was significantly less in the NP–C PNs (Fig. 6d). VEGF/NP–C PNs showed similar pattern in LC3-II and p62 increase compared with WT cells (Fig. 6d). Taken together, these

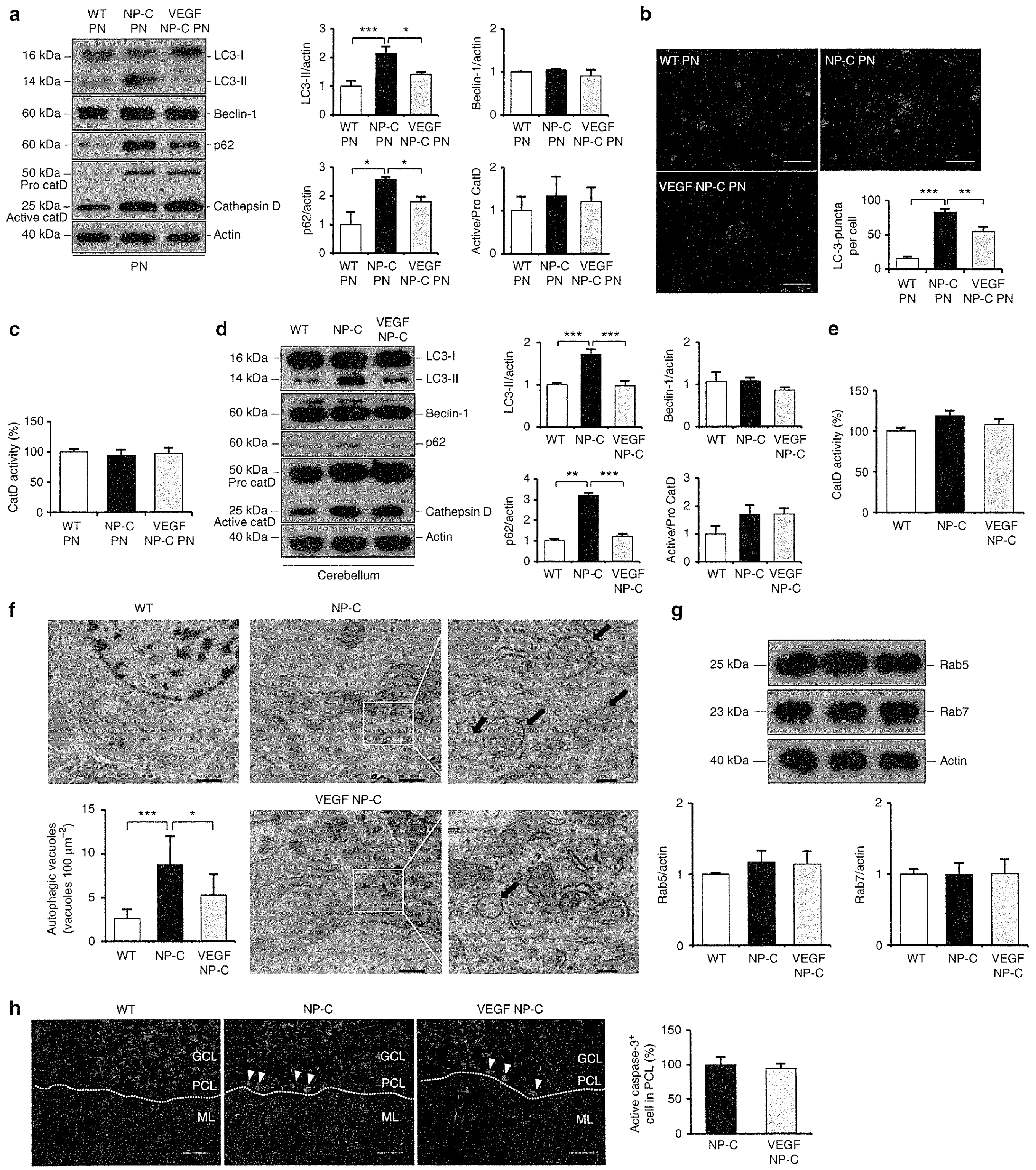

Figure 5 | VEGF replenishment reverses defective autophagy in NP-C mice. (**a**) Western blot analysis of LC3, beclin-1, p62 and cathepsin D in primary cultured PNs derived from WT, NP-C and VEGF/NP-C mice (WT, $n=5$; NP-C, $n=6$; and VEGF/NP-C, $n=6$). (**b**) Immunocytochemistry of LC3 in WT, NP-C and VEGF/NP-C PNs ($n=6$ per group; scale bar, 20 μm). (**c**) Cathepsin D activity in primary cultured PNs (WT, $n=5$; NP-C, $n=6$; and VEGF/NP-C, $n=6$). (**d**) Western blot analysis of LC3, beclin-1, p62 and cathepsin D in the cerebellums of 6-week-old WT, NP-C and VEGF/NP-C mice (WT, $n=6$; NP-C, $n=7$; and VEGF/NP-C, $n=7$). (**e**) Cathepsin D activity in the cerebellums of WT, NP-C and VEGF/NP-C mice (WT, $n=5$; NP-C, $n=6$; and VEGF/NP-C, $n=6$). (**f**) EM images and quantification data of the cerebellum ($n=5$ per group; low-magnification scale bar, 1 μm; high-magnification scale bar, 200 nm). Arrow indicates autophagic vacuole. (**g**) Western blot analysis of Rab5 and Rab7 levels in the cerebellum ($n=6$ per group). (**h**) Cerebellar sections were immunostained with anti-active caspase-3 and the number of active caspase-3-positive cells in PCL was quantified ($n=5$ per group; scale bar, 50 μm). **a**-**g**, one-way analysis of variance, Tukey's *post hoc* test. **h**, Student's *t*-test. $^{*}P<0.05$, $^{**}P<0.01$, $^{***}P<0.005$. All error bars indicate s.e.m.

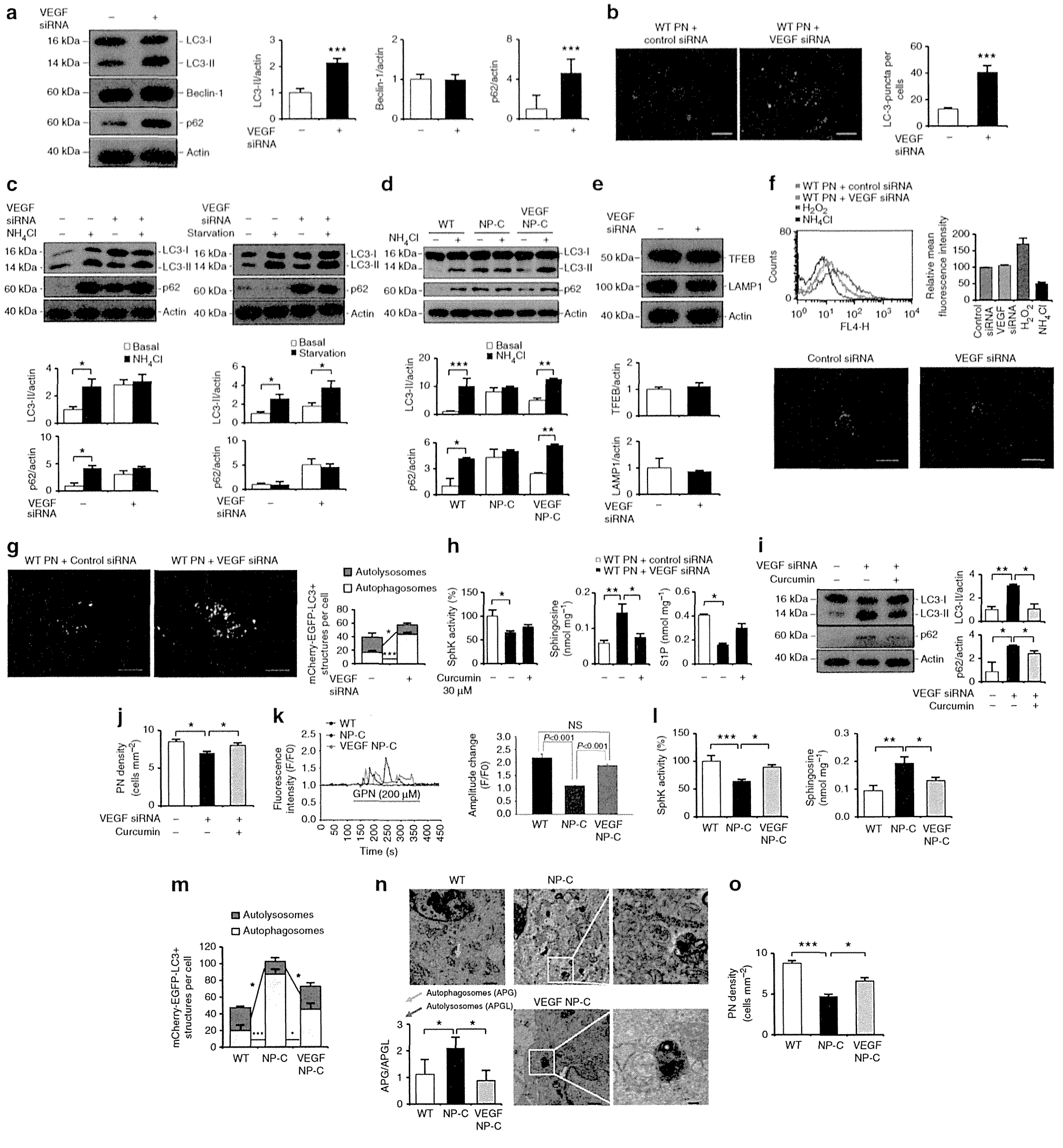

Figure 6 | VEGF/SphK inactivity impairs autophagic flux. (**a**) Western blots of LC3, beclin-1 and p62 in PNs after VEGF knockdown (*n* = 6 per group). (**b**) Immunocytochemistry of LC3 in PNs after VEGF knockdown (*n* = 6 per group; scale bar, 20 μm). (**c**) Autophagic flux assay. Western blots of LC3 and p62 in PNs (*n* = 6 per group). (**d**) Western blots of LC3 and p62 in cultured PNs in the presence of NH_4Cl (*n* = 5 per group). (**e**) Western blots of TFEB and Lamp1 in VEGF-knockdown PNs (control, *n* = 5 and VEGF siRNA, *n* = 6). (**f**) Effect of VEGF knockdown on lysosomal pH. PNs stained with LysoTracker red (*n* = 5 per group; scale bar, 20 μm). (**g**) Fluorescence analysis of autophagosomes and autolysosomes (control, *n* = 7 and VEGF siRNA, *n* = 8; scale bar, 10 μm). (**h**) Sphk activity, sphingosine and S1P levels in PNs after VEGF knockdown in the presence of curcumin (*n* = 8 per group). (**i**) Western blot analysis of LC3 and p62 in VEGF-knockdown PNs treated with curcumin (control, *n* = 7; VEGF siRNA, *n* = 8; and VEGF siRNA/curcumin, *n* = 8). (**j**) Survival of VEGF-knockdown PNs treated with curcumin (*n* = 8 per group). (**k**) Left, representative traces showing intracellular [Ca^{2+}] changes monitored in single fluo-4-loaded PNs. Right, maximal peak fluorescence changes were determined as the differences between basal and the maximum fluorescence (*n* = 10 cells per group). (**l**) Sphk activity and sphingosine levels were measured in cultured PNs (*n* = 8 per group). (**m**) Quantification of autophagosomes and autolysosomes in primary cultured PNs (WT, *n* = 7; NP-C, *n* = 7; and VEGF/NP-C, *n* = 8). (**n**) EM analysis of the PNs (*n* = 5 per group; low-magnification scale bar, 1 μm; high-magnification scale bar, 200 nm). (**o**) Survival of primary cultured PNs (WT, *n* = 6; NP-C, *n* = 8; and VEGF/NP-C, *n* = 8). **a**,**b**,**e**,**g**, Student's *t*-test. **c**,**d**,**f**,**h**-**o**, one-way analysis of variance, Tukey's *post hoc* test. *$P < 0.05$, **$P < 0.01$, ***$P < 0.005$. All error bars indicate s.e.m.

results indicated that reduced VEGF levels in NP–C PNs caused a defect of autophagic degradation, but not induction.

Our findings that depletion of VEGF affects autophagic degradation prompted us to more closely examine how VEGF might influence in defective autophagic degradation. We first examined the transcription factor EB (TFEB), which coordinates lysosomal formation[24]. VEGF depletion in WT PNs did not affect the levels of TFEB and Lamp1, indicating that VEGF did not impair lysosome biogenesis (Fig. 6e). Next, we assessed alteration in lysosomal pH using the acidotropic dye LysoTracker red. H_2O_2- and NH_4Cl-treated cells were used as positive and negative controls, respectively. VEGF siRNA-treated PNs exhibited a similar fluorescence to control siRNA-treated PNs, indicating that VEGF did not affect lysosomal acidification (Fig. 6f).

Following the initiation of the phagophores, autophagosomes undergo a stepwise maturation process from early to late autophagosomes, which ultimately fuse with lysosomes to form autolysosomes. To study the effect of VEGF depletion on the maturation of autophagosomes, we used mCherry-EGFP-LC3 reporter[25]. Before fusion with lysosomes, the LC3-II-positive autophagosomes are shown by both GFP and mCherry signals as yellow puncta, and after fusion, autolysosomes are shown by only mCherry signals as red-only puncta because GFP loses its fluorescence in acidic pH. Compared with control PNs, VEGF siRNA-treated cells showed significantly increased yellow puncta (autophagosomes) and decreased mCherry-only puncta (autolysosomes), indicating that VEGF depletion inhibited the autophagosome–lysosome fusion (Fig. 6g).

Sphingosine accumulation can induce defective calcium release from the acidic compartment such as lysosome, which inhibits fusion of lysosome with other organelles[4]. As shown in Supplementary Figs 2g and 3h, decreased VEGF levels caused sphingosine accumulation in WT PNs. Thus, we hypothesized that defective lysosomal calcium release by VEGF-mediated sphingosine accumulation disturbs autophagosome–lysosome fusion and evokes the abnormal autophagosomes' amassment. To test this hypothesis, we used the weaker sarcoplasmic reticulum ATPase antagonist curcumin, a natural product derived from turmeric[26], which correct sphingolipid imbalance by increasing the cytosolic calcium release[4]. Importantly, abnormal sphingolipid levels in the VEGF siRNA-treated PNs were normalized after curcumin treatment (Fig. 6h). We also observed significantly decreased protein level of abnormal autophagic markers (Fig. 6i) and increased neuronal survival (Fig. 6j) in the VEGF-knockdown PNs after curcumin treatment compared with PNs with VEGF knockdown alone. Similar results were observed in the VEGF shRNA-treated mice after curcumin injection (Supplementary Fig. 6). To further examine these effects, we analysed calcium homeostasis in the primary cultured PNs derived from WT, NP–C and VEGF/NP–C mice. To specifically assess the lysosomal calcium content, we used Gly-Phe β-naphthylamide (GPN), which osmotically lyses cathepsin-containing lysosome[4]. We observed a reduction in NP–C PNs' calcium release from lysosome compared with WT PNs, consistent with our previous study[7]. Notably, this reduction was corrected in VEGF/NP–C PNs (Fig. 6k). As expected, abnormal sphingosine accumulation was reduced in VEGF/NP–C cells by restoration of SphK activity (Fig. 6l). Moreover, VEGF/NP–C PNs showed decreased autophagosome (yellow LC3 puncta) accumulation (Fig. 6m). Decreased autophagosomes in the VEGF/NP–C PNs were further confirmed by EM analysis (Fig. 6n). The survival of PNs was also significantly increased in the VEGF/NP–C (Fig. 6o). Together, these findings show that inactivated VEGF/SphK pathway in NP–C PNs causes sphingosine accumulation and this amassment inhibits autophagosome–lysosome fusion by disturbance of calcium homeostasis.

VEGF rescues autophagic defects in patient-specific cells. To further validate our observation regarding VEGF treatment in NP–C mice, we studied effects of VEGF on SphK activity in human NP–C fibroblasts. Human NP–C fibroblasts cocultured with human BM-MSCs, VEGF^{tg} BM-MSCs or treated with recombinant VEGF showed significantly increased SphK activity, decreased sphingosine and elevated S1P (Supplementary Fig. 7a–c). Increased LC3-II levels and p62 accumulation in NP–C fibroblasts were reduced by VEGF treatment (Supplementary Fig. 7d,e). VEGF-treated NP–C fibroblasts also showed increased calcium release and decreased autophagosome accumulation (as judged by yellow LC3 puncta) compared with non-treated NP–C fibroblasts (Supplementary Fig. 7f,g). Lysosomal exocytosis is necessary to affect clearance of stored intracellular lipids and ameliorates the endolysosomal lipid storage phenotype in NP–C cells[27]. To determine whether VEGF directly induced lysosomal exocytosis, the culture media of normal and NP–C fibroblasts treated with or without VEGF were analysed for the presence of the lysosomal enzyme β-hexosaminidase as a marker for lysosomal content secretion. In all groups, the activity of β-hexosaminidase was not significantly elevated at the indicated times (Supplementary Fig. 7h). The low-level appearance of β-hexosaminidase in the culture media of fibroblasts is not a result of generalized cell lysis, since the levels of lactate dehydrogenase (LDH) in the media remained unchanged in all groups for the duration of the assay (Supplementary Fig. 7h). These results suggested that the ability of

Figure 7 | VEGF ameliorates sphingolipid imbalance in NP-C iPSC neurons. (**a**) Left, normal, hNPC-3 and hNPC-17 iPSCs generated nestin-positive neuroprogenitor cells (scale bar, 50 μm). Right, representative images of immunocytochemical staining the β-III tubulin following neural differentiation (scale bar, 50 μm). (**b**) hNPC-3 and hNPC-17 neurons were treated with human BM-MSCs, VEGF^{tg} BM-MSCs or recombinant VEGF (10 ng ml^{-1}). Three days after treatment, VEGF levels were measured in cell lysates. (**c**-**f**) SphK activity (**c**), sphingosine (**d**), S1P (**e**) and sphingomyelin (**f**) were measured in normal iPSC neurons and hNPC neurons with or without treatment. (**g**) Filipin staining of unesterified cholesterol in hNPC-3 neurons with or without treatment of recombinant VEGF for 3 days (scale bar, 50 μm). Quantification of filipin fluorescence intensities normalized to normal neurons. Unesterified cholesterol levels in normal iPSC neurons and hNPC neurons with or without treatment were measured ($n=6$ per group). (**h**) Effect of the VEGFR2 inhibitor on VEGF mediated sphingolipid modulation. hNPC-3 neurons were pretreated with PTK787 at 10 μM for 1 day and were treated for 3 days with 10 ng ml^{-1} VEGF and then assayed for SphK activity, sphingosine and S1P ($n=7$ per group). (**i**,**j**) Effect of NPC1 knockdown on sphingolipid factors in normal iPSC neurons. (**i**) Three days after NPC1 siRNA transfection, we measured the levels of *NPC1* mRNA and VEGF expression. (**j**) SphK activity, sphingosine and S1P were measured in normal iPSC neurons treated with control or NPC1 siRNA (control, $n=7$; NPC1 siRNA, $n=9$). (**k**) Effect of VEGF knockdown on sphingolipid factors in normal iPSC neurons. Three days after VEGF siRNA transfection, we measured the levels of *VEGF* mRNA, SphK activity, sphingosine and S1P in normal iPSC neurons ($n=7$ per group). (**l**) Effect of a specific SphK1 inhibitor on sphingolipid factors in normal iPSC neurons. Normal neurons were treated with or without 20 μM SK1-I for 6 h. Lipids were extracted and sphingosine, S1P and unesterified cholesterol levels were determined ($n=6$ per group). **b**-**h**, one-way analysis of variance, Tukey's *post hoc* test. **i**-**l**, Student's *t*-test. $^*P<0.05$, $^{**}P<0.01$, $^{***}P<0.005$. All error bars indicate s.e.m.

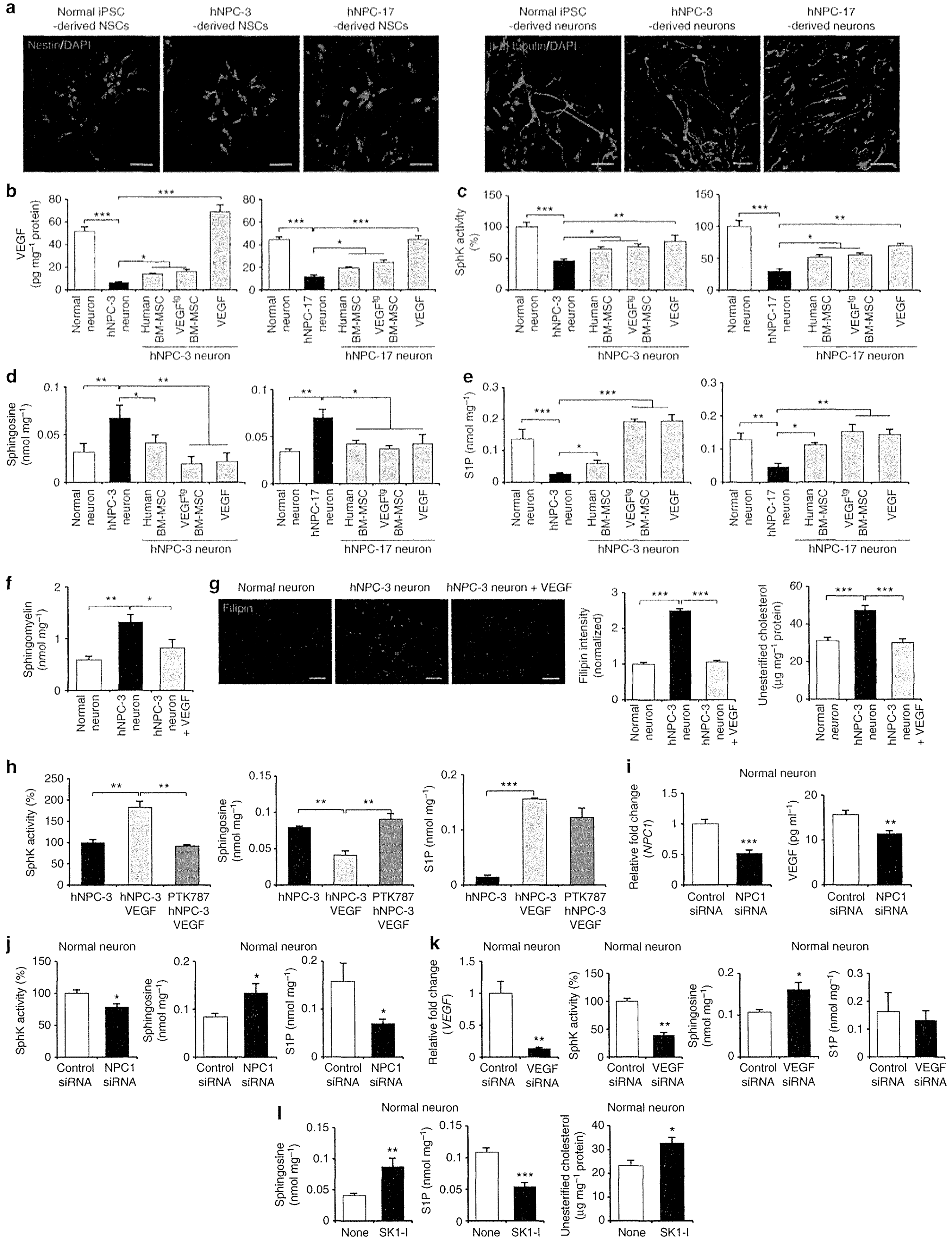
a
Normal iPSC -derived NSCs
hNPC-3 -derived NSCs
hNPC-17 -derived NSCs
Nestin/DAPI
Normal iPSC -derived neurons
hNPC-3 -derived neurons
hNPC-17 -derived neurons
βIII tubulin/DAPI
b
VEGF (pg mg^{-1} protein)
Normal neuron
hNPC-3 neuron
Human BM-MSC
VEGF^{tg} BM-MSC
VEGF
hNPC-3 neuron
hNPC-17 neuron
hNPC-17 neuron
c
SphK activity (%)
d
Sphingosine (nmol mg^{-1})
e
S1P (nmol mg^{-1})
f
Sphingomyelin (nmol mg^{-1})
hNPC-3 neuron + VEGF
g
Normal neuron
hNPC-3 neuron
hNPC-3 neuron + VEGF
Filipin
Filipin intensity (normalized)
Unesterified cholesterol (μg mg^{-1} protein)
h
SphK activity (%)
Sphingosine (nmol mg^{-1})
S1P (nmol mg^{-1})
hNPC-3
hNPC-3 VEGF
PTK787 hNPC-3 VEGF
i
Normal neuron
Relative fold change (NPC1)
VEGF (pg ml^{-1})
Control siRNA
NPC1 siRNA
j
Normal neuron
SphK activity (%)
Sphingosine (nmol mg^{-1})
S1P (nmol mg^{-1})
Control siRNA
NPC1 siRNA
k
Normal neuron
Relative fold change (VEGF)
SphK activity (%)
Sphingosine (nmol mg^{-1})
S1P (nmol mg^{-1})
Control siRNA
VEGF siRNA
l
Normal neuron
Sphingosine (nmol mg^{-1})
S1P (nmol mg^{-1})
Unesterified cholesterol (μg mg^{-1} protein)
None
SK1-I
*
**
***

VEGF to reduce sphingosine storage in NP–C cells was not due to lysosomal exocytosis.

The recent developments in induced pluripotent stem cells (iPSCs) and iPSC-derived neurons have allowed investigation of pathogenesis of neurological diseases *in vitro*. To explore whether the observed effects of VEGF we describe above were similar in NP–C human neurons, we established human NP–C iPSCs (hNPC-3, 6, 17) by transduction of human NP–C fibroblasts with retroviruses encoding *OCT4*, *SOX2*, *KLF4* and *c-MYC* similar to previous studies[28–30]. Analysis of NP–C iPSCs (hNPC-3) revealed typical characteristics of pluripotent stem cells: similar morphology to embryonic stem cells (ES cells), expression of pluripotent markers including SSEA-4, Tra-1-60 and Tra-1-81, normal chromosomal number and genomic structure, silencing of retroviral transgene and reactivation of genes indicative of pluripotency (Supplementary Fig. 8a–c). The differentiation ability of NP–C iPSCs was also confirmed *in vivo* by teratoma formation (Supplementary Fig. 8d). We analysed SphK activity and sphingolipid levels in the normal iPSC and NP–C iPSC lines. NP–C iPSC lines exhibited decreased SphK activity, increased sphingosine accumulation and decreased S1P levels compared with normal iPSCs (Supplementary Fig. 8e).

Next, human neurons were induced from the hNPC-3, hNPC-17 and normal iPSC. Early-differentiating cells expressed nestin and differentiated cells expressed neuron-specific β-III tubulin (Fig. 7a). These NP–C neurons also exhibited phenotypes seen in human NP–C samples, including abnormal VEGF levels and sphingolipid metabolism (Fig. 7b–e). To confirm the effects of VEGF in human NP–C neurons, the hNPC-3- or hNPC-17-derived neurons were cocultured with human or VEGF^{tg} BM-MSCs, or treated with recombinant VEGF. We found that all treated groups exhibited increased VEGF, elevated SphK activity, decreased sphingosine accumulation and increased S1P levels (Fig. 7b–e). Sphingomyelin and unesterified cholesterol levels were also significantly decreased in VEGF-treated NP–C neurons (Fig. 7f,g). We also pretreated NP–C neurons with PTK787 before VEGF treatment. We found that SphK activity and other sphingolipid metabolites in NP–C neurons were mediated by interactions of VEGF and its receptor VEGFR2 in these iPSC-derived NP–C neurons (Fig. 7h).

To reconfirm the *in vitro* mechanism whereby there is a direct relationship between *NPC1*, VEGF and SphK activity in human neurons, we treated normal iPSC neurons with NPC1 and VEGF siRNA (Fig. 7i–k) and determined changes in various sphingolipid factors. NPC1 siRNA decreased VEGF expression and SphK activity (Fig. 7i,j). VEGF siRNA also strongly inactivated SphK levels (Fig. 7k). Both siRNA treatments led to changed levels of sphingosine and S1P, similar to NP–C neurons (Fig. 7j,k). To determine whether reduction in SphK activity affected sphingolipid factors and unesterified cholesterol in iPSC neurons similar to those in classical NP–C cells, we treated the normal iPSC neurons with a specific SphK1 inhibitor, SK1-I. We found that inhibition of SphK activity increased sphingosine and unesterified cholesterol accumulation and decreased cellular S1P (Fig. 7l).

We also examined whether NP–C neurons exhibited abnormal autophagy. NP–C neurons had significantly higher abnormal autophagic markers than normal neurons (Fig. 8a). VEGF treatment significantly decreased the protein level of abnormal autophagic markers in NP–C neurons (Fig. 8a). Similar to previous results (Supplementary Fig. 7), VEGF-treated NP–C neurons showed increased calcium release and decreased autophagosome accumulation, suggesting that VEGF elevates autophagosome–lysosome fusion (Fig. 8b–d). Consistent with the restored autophagy flux, cell survival was also significantly improved in VEGF-treated NP–C neurons (Fig. 8e). Collectively, these results confirm that defective autophagy by abnormal VEGF/SphK pathway and sphingosine levels in NP–C mice and human fibroblasts also occur in NP–C patient neurons, and replenishment of VEGF is able to ameliorate autophagy defect by correction of sphingolipid imbalance in the NP–C patient cells.

Discussion

NP–C patients and mice exhibit progressive neuronal loss, mainly of cerebellar PNs, but the mechanism is largely unknown. Recent studies have shown that inactivation of NPC1 caused abnormal autophagy and the defect may contribute to PN loss in NP–C[22]. Loss of NPC1 function leads to trapping of lipids within aberrant membrane compartments, and this may induce a 'lipid-starvation response' analogous to the well-characterized autophagic response to amino-acid deprivation[31]. In addition, destructive autophagy in NP–C PNs may also be stimulated hormonally via neurosteroids. Neurosteroids might inhibit autophagy in PNs and when their synthesis is severely decreased, as in NP–C[32], autophagic cell death might ensue. Similar to previous results[22,33], we found that the impaired autophagic flux in NP–C was associated with decreased autophagosome–lysosome fusion, and that this defect led to PNs loss.

Recent studies have also demonstrated that cholesterol, sphingomyelin and GSL storage are downstream events in NP–C disease pathogenesis caused by sphingosine storage, leading to altered acidic compartment calcium levels[4]. They

Figure 8 | VEGF rescues the autophagic defects in NP-C iPSC neurons. (**a**) Western blot analysis of LC3 and p62 in normal and NP-C iPSC-derived neurons treated with or without 10 ng ml^{-1} recombinant VEGF (normal, $n=6$; hNPC, $n=7$; and VEGF-treated hNPC, $n=7$). (**b**) Left, representative traces showing intracellular [Ca^{2+}] changes monitored in single fluo-4-loaded normal and NP-C iPSC neurons treated with or without recombinant VEGF (10 ng ml^{-1}). Right, maximal peak fluorescence changes were determined as the differences between basal and the maximum fluorescence, on addition of 200 μM GPN ($n=10$ cells per group). (**c**) Fluorescence staining and quantification of autophagosomes (mCherry^{+}-EGFP^{+}-LC3) and autolysosomes (mCherry^{+}-EGFP^{-}-LC3) in normal and NP-C iPSC neurons after recombinant VEGF treatment (normal, $n=7$; hNPC, $n=8$; and VEGF-treated hNPC, $n=8$; scale bar, 10 μm). (**d**) EM images and quantification data of normal and NP-C iPSC-derived neurons after 10 ng ml^{-1} VEGF treatment ($n=5$ per group; low-magnification scale bar, 1 μm; high-magnification scale bar, 200 nm). (**e**) Quantification of cell viability (normal, $n=5$; hNPC, $n=6$; and VEGF-treated hNPC, $n=6$). (**f**) Model of VEGF-mediated SphK activation in NP-C neurons. (A,B) In NP-C cells, sphingosine accumulation is increased due to defective SphK activity together with decreased VEGF caused by mutated NPC1 and defective uptake via VEGFR2. (C) Abnormal sphingosine accumulation decreases calcium release from lysosomes and the reduction in calcium release causes an autophagic defect by inhibiting autophagosome-lysosome fusion. Eventually, these defects cause loss of cerebellar neurons. (D,E) When NP-C neurons are exposed to BM-MSCs or pure VEGF, the cells exhibit elevated intracellular levels of VEGF (F), which induces VEGFR2-mediated activation of SphK in the cytosol and lysosome. (G) This activation leads to decreased sphingosine accumulation and increased S1P levels. (H) Reduced sphingosine accumulation results in improved autophagosome-lysosome fusion by correction of calcium homeostasis. Finally, this restoration prevents neuronal loss in NP-C. **a**-**e**, one-way analysis of variance, Tukey's *post hoc* test. $^{*}P<0.05$, $^{**}P<0.01$, $^{***}P<0.005$. All error bars indicate s.e.m.

have determined the chronology of events after inactivation of NPC1. In a drug-induced NP–C cellular model, sphingosine storage in the acidic compartment led to calcium depletion in these organelles, which then resulted in cholesterol, sphingomyelin and GSL storage in these compartments. Therefore, sphingosine storage might be an initiating factor in NPC1 disease pathogenesis that causes altered calcium homeostasis, leading to the secondary storage of sphingolipids and cholesterol, although additional studies are required. Similarly, we found that VEGF-mediated sphingosine modulation also significantly decreased sphingomyelin and unesterified cholesterol levels. Therefore, we suggest that